

**GSFC JPSS CMO
December 5, 2011
Released**

**Joint Polar Satellite System (JPSS) Ground Project
Code 474
474-00050**

**Joint Polar Satellite System (JPSS)
VIIRS Atmospheric Correction Over Ocean
Algorithm Theoretical Basis Document
(ATBD)**

For Public Release

The information provided herein does not contain technical data as defined in the International Traffic in Arms Regulations (ITAR) 22 CFC 120.10. This document has been approved For Public Release to the NOAA Comprehensive Large Array-data Stewardship System (CLASS).



National Aeronautics and
Space Administration

**Goddard Space Flight Center
Greenbelt, Maryland**

This page intentionally left blank.

Joint Polar Satellite System (JPSS) VIIRS Atmospheric Correction Over Ocean Algorithm Theoretical Basis Document (ATBD)

JPSS Electronic Signature Page

Prepared By:

Neal Baker
JPSS Data Products and Algorithms, Senior Engineering Advisor
(Electronic Approvals available online at https://jpssmis.gsfc.nasa.gov/mainmenu_dsp.cfm)

Approved By:

Heather Kilcoyne
DPA Manager
(Electronic Approvals available online at https://jpssmis.gsfc.nasa.gov/mainmenu_dsp.cfm)

**Goddard Space Flight Center
Greenbelt, Maryland**

This page intentionally left blank.

Preface

This document is under JPSS Ground AERB configuration control. Once this document is approved, JPSS approved changes are handled in accordance with Class I and Class II change control requirements as described in the JPSS Configuration Management Procedures, and changes to this document shall be made by complete revision.

Any questions should be addressed to:

JPSS Ground Project Configuration Management Office
NASA/GSFC
Code 474
Greenbelt, MD 20771

This page intentionally left blank.

Change History Log

Revision	Effective Date	Description of Changes (Reference the CCR & CCB/ERB Approve Date)
Original	04/22/2011	474-CCR-11-0065: This version baselines D43314, VIIRS Atmospheric Correction Over Ocean Algorithm Theoretical Basis Document ATDB (REF Y2389), Rev D dated 07/15/2010 as a JPSS document, version Rev -. This is the version that was approved for NPP launch. Per NPOESS CDFCB - External, Volume V – Metadata, doc number D34862-05, this has been approved for Public Release into CLASS. This CCR was approved by the JPSS Algorithm ERB on April 22, 2011.

This page intentionally left blank.

Northrop Grumman Space & Mission Systems Corp.
Space Technology
One Space Park
Redondo Beach, CA 90278

NORTHROP GRUMMAN

Raytheon



**Engineering & Manufacturing Development (EMD) Phase
Acquisition & Operations Contract**

CAGE NO. 11982

**VIIRS Atmospheric Correction Over Ocean
Algorithm Theoretical Basis Document ATBD (ref Y2389)**

Document Date: 7/15/2010

**Document Number: D43314
Revision: D**

Point of Contact: Nancy Andreas

ELECTRONIC APPROVAL SIGNATURES:



Prepared by
Northrop Grumman Space Technology
One Space Park
Redondo Beach, CA 90278

Prepared for
Department of the Air Force
NPOESS Integrated Program Office
C/O SMC/CIK
2420 Vela Way, Suite 1467-A8
Los Angeles AFB, CA 90245-4659

Under
Contract No. F04701-02-C-0502

COMMERCE DESTINATION CONTROL STATEMENT

The export of these commodities, technology or software are subject to the U.S. Export Laws and Regulations in accordance with the Export Administration Regulations. Diversion contrary to U.S. law is prohibited.

Northrop Grumman Space & Mission Systems Corp. Space Technology One Space Park Redondo Beach, CA 90278		 	
Revision/Change Record			Document Number D43314
Revision	Document Date	Revision/Change Description	Pages Affected
---	1/18/2007	Initial PCIM Release to bring document into Matrix Accountability. Reference original document number: Y2389 delivered in 2005	All
A	1/6/2008	Update for SPCR ALG00001234	p. i – p. 9
B	2/18/2009	Updated according to CSR RFA SY_139 with NGST SPCR ALG00001362 under ECR A-199	Most pages
C	5/12/2010	Updated with NGST SPCR ALG00001544 under ECR A-295 for Drop 4.24	Most pages
D	7/15/2010	Resolved TBD according to NGAS SPCR ALG00001638 under ECR A-319	Title page, change page, pages vii and 24



Raytheon

**ATMOSPHERIC CORRECTION OVER OCEAN
FOR PRODUCTION OF REMOTE SENSING REFLECTANCE
INTERMEDIATE PRODUCT
VISIBLE/INFRARED IMAGER/RADIOMETER SUITE
ALGORITHM THEORETICAL BASIS DOCUMENT**

Version 5 Revision 7: August 2005

Quanhua Liu
Corinne Carter

*Kendall Carder, Science Team Member
University of South Florida*

RAYTHEON SYSTEMS COMPANY
Information Technology and Scientific Services
4400 Forbes Boulevard
Lanham, MD 20706

SBRS Document #: Y2389

Revision/Change Record**For Document No. Y2389**

Symbol	Document Date	Authorization Date	Revision/Change Description	Pages Affected
	8/23/2005	Justin Ip	SPCR ALG00000018	Most pages
	2/27/2003	Justin Ip	SPCR ALG00000029, NP-EMD.03.591.009 (assigned) NP-EMD.03.591.009 (closed)	p. ix, 1, 3, 4, 5, 7, 16, 17, 18, 19, 22, 35, 36, 38, 39
	2/19/2003	Justin Ip	SPCR ALG00000022, NP-EMD.03.591.005 (assigned) NP-EMD.03.591.007 (closed)	p. 5

SDR: ATMOSPHERIC CORRECTION OVER OCEAN

Doc No: Y2389

Version: 5

Revision: 7

	FUNCTION	NAME	SIGNATURE	DATE
Prepared By	EDR Developer	Q. LIU		1/25/02
Approved By	Relevant IPT Lead	D. HOMMEL		2/1/02
Approved By	Chief Scientist	S. MILLER		2/8/02
Released By	Algorithm IPT Lead	P. KEALY		2/15/02

TABLE OF CONTENTS

	<u>Page</u>
TABLE OF CONTENTS	i
LIST OF FIGURES	iii
LIST OF TABLES	v
GLOSSARY OF ACRONYMS	vi
ABSTRACT	vii
1.0 INTRODUCTION	1
1.1 PURPOSE	1
1.2 SCOPE	1
1.3 VIIRS DOCUMENTS	1
1.4 REVISIONS	1
2.0 EXPERIMENT OVERVIEW	3
2.1 OBJECTIVES OF ATMOSPHERIC CORRECTION OVER OCEAN	3
2.2 INSTRUMENT CHARACTERISTICS	3
2.3 RETRIEVAL STRATEGY	4
3.0 ALGORITHM DESCRIPTION	5
3.1 PROCESSING OUTLINE	5
3.2 ALGORITHM INPUT	5
3.2.1 VIIRS Data	5
3.2.2 Non-VIIRS Data	5
3.3 THEORETICAL DESCRIPTION OF ATMOSPHERIC CORRECTION OVER OCEAN RETRIEVALS	6
3.3.1 Physics of the Problem	6
3.3.2 Mathematical Description of the Algorithm	8
3.3.3 Diffuse Transmittance	15
3.3.4 Aerosol effect	16
3.3.5 Sun glint mask and correction	19
3.3.6 Algorithm Output	20
3.3.7 Variance and Uncertainty Estimates	22
3.4 ALGORITHM SENSITIVITY STUDIES	24
3.4.1 Calibration Errors	24
3.4.2 Instrument Noise	24
3.4.3 Stray light effect	28
3.4.4 Residual instrumental polarization	33
3.4.5 Absorbing aerosols	39
3.5 PRACTICAL CONSIDERATIONS	40
3.5.1 Numerical Computation Considerations	40

3.5.2	Correction to the Instrumental Polarization.....	40
3.5.3	Stray Light Warning Flag	41
3.5.4	Programming and Procedural Considerations	41
3.5.5	Quality Assessment and Diagnostics.....	41
3.5.6	Exception Handling	41
3.6	ALGORITHM VALIDATION.....	41
3.6.1	Error Budget	41
3.6.2	Global maps of remote sensing reflectance and retrieval of chlorophyll	42
3.6.3	Post-launch validation	43
3.7	ALGORITHM DEVELOPMENT ACTIVITIES (P ³ I).....	44
4.0	ASSUMPTIONS AND LIMITATIONS	45
4.1	ASSUMPTIONS.....	45
4.2	LIMITATIONS.....	45
5.0	ACKNOWLEDGEMENTS.....	46
6.0	REFERENCES	47

LIST OF FIGURES

	<u>Page</u>
Figure 1. VIIRS band position and width. Solid line represents the Rayleigh optical thickness. The dashed line indicates the optical thickness of gases. In this figure, the right-hand dark box represents the old band centered at 751 nm, which was later adjusted to reduce the influence of the adjacent O ₂ absorption feature.	4
Figure 2. Algorithm flow diagram adapted from Gordon (1996).	7
Figure 3. Simulated TOA radiance from the modified MODTRAN radiative transfer model. The light gray part represents the atmospheric contribution. The gray part is the contribution from air-sea interface. The dark gray indicates the water-leaving radiance.	Error! Bookmark not defined.
Figure 4. Spectral variation of the water-leaving radiances measured by the high-resolution spectrographs on MOBY.	9
Figure 5. Schematic drawing of the radiation transport.	16
Figure 7a. Comparison of the diffuse transmittance from our derivation and the detailed radiative transfer calculation.	Error! Bookmark not defined.
Figure 7b. Variation of the phase function with the scattering angle.	17
Figure 7c. Values of $\epsilon(\lambda, 858)$ for nadir viewing with $\theta_0=60^\circ$ for the maritime, costal, and tropospheric aerosol models. For each model, the relative humidity values are 50, 70, 90, and 99% from the top to the bottom curves.	18
Figure 8. Sun glint (red color) area for a wind speed of 8 m s ⁻¹ for simulated 1330 VIIRS orbit.	19
Figure 10. Mean chlorophyll precision due to sensor noise in the VIIRS near-IR bands as a function of VIIRS sensor performance model number. The precision values are averages for a 2400 km wide swath and solar zenith angle less than 70 degrees. The dashed line indicates the threshold requirement of 20 percent. The numbers on the x- axis represent models with worsening signal to noise ratio as the sensor model number increases. The Raytheon VIIRS final sensor noise level is between that given by sensor models 2 and 3.	26
Figure 11. Mean chlorophyll precision due to sensor noise in the VIIRS visible bands as a function of VIIRS sensor performance model number. The precision values are averages for a 2400 km wide swath and solar zenith angle less than 70 degrees. The dashed line indicates the threshold requirement of 20 percent. The numbers on the x- axis represent models with worsening signal to noise ratio as the sensor model number increases. The Raytheon VIIRS final sensor is between that given by sensor models 2 and 3.	27
Figure 12. Chlorophyll precision due to sensor noise, averaged over the viewing swath of the 1:30 PM orbit, as a function of VIIRS sensor performance model. The results for atmospheric correction using the 745-785 nm and 841-876 nm band	

pair are shown as diamonds. The results using the 743-753 nm and 841-876 nm band pair are shown as crosses.	27
Figure 13. Chlorophyll accuracy as a function of a distance from the edge of a semi-infinite cloud. A dashed line represents the accuracy of 10% allocated for the stray light error source.	30
Figure 14. Comparison of the chlorophyll accuracy obtained with no atmospheric correction and the Gordon-Wang atmospheric correction algorithm. A dashed line represents the accuracy of 10% allocated for the stray light error source.	31
Figure 15. Comparison of the chlorophyll accuracy calculated for a semi-infinite cloud, desert, and vegetation. The Gordon-Wang atmospheric correction algorithm was applied to the TOA radiances.	32
Figure 16. Comparison of the chlorophyll accuracy calculated for the semi-infinite and limited clouds using the Gordon-Wang atmospheric correction.	33
Figure 17. Degree of polarization at 443 nm.	36
Figure 18. Variation of linear polarization with the optical depth of the aerosol.	37
Figure 19. Sun zenith = 41°, viewing = 30°, Relative azimuth = 90°, chlorophyll = 0.1 mg/m ³	38
Figure 20. Retrieval uncertainty for various polarization sensitivities. The two-step algorithm yields the best results.	39
Figure 21. Variation of $\epsilon(\lambda, 865)$ for nadir viewing with a sun zenith angle of 41° for the maritime, continental and urban aerosol models for RH=50% and a desert aerosol (wintertime) with RH=0%.	40
Figure 22. Retrieved remote sensing reflectance.	43
Figure 23. Uncertainty of the retrieval of the chlorophyll concentration.	43

LIST OF TABLES

	<u>Page</u>
Table 1. VIIRS Visible and Near-infrared Bands	3
Table 2. The 12 aerosol models used in the VIIRS ACO algorithm.....	3

GLOSSARY OF ACRONYMS

3-D	Three-dimensional
6S	Second Simulation of the Satellite Signal in the Solar Spectrum
ACO	Atmospheric Correction Over Ocean
ATBD	Algorithm Theoretical Basis Document
EDR	Environmental Data Record
IP	Intermediate Product
MM5	Mesoscale Model, version 5
MOBY	Marine Optical Buoy
MODIS	Moderate Resolution Imaging Spectroradiometer
MODTRAN	Moderate Resolution Atmospheric Radiance and Transmittance Model
NIR	Near-Infrared
OCC	Ocean Color/Chlorophyll
OMPS	Ozone Mapping Profiling Suite
PSF	Point Spread Function
RSR	Remote-Sensing Reflectance
SeaWiFS	Sea-viewing, Wide Field-of-view Sensor
TOA	Top of Atmosphere
VIIRS	Visible/Infrared Imager/Radiometer Suite

ABSTRACT

This Algorithm Theoretical Basis Document (ATBD) describes the atmospheric correction over ocean algorithm developed by Gordon and Wang (1994a) for use on the Sea-viewing Wide Field-of-view Sensor (SeaWiFS) and the Moderate Resolution Imaging Spectroradiometer (MODIS) data. A polarized radiative transfer model extends the algorithm, accounting for the residual instrumental polarization sensitivity. Inputs to the algorithm are measured Visible/Infrared Imager/Radiometer Suite (VIIRS) radiances in the visible and near-infrared (NIR) bands (M1-M7), sea surface wind speed, surface atmospheric pressure, total precipitable water, and total ozone column. The algorithm subtracts the radiance contributions due to molecular and aerosol scattering in the atmosphere, and reflection from the air-sea interface, from the measured VIIRS radiances. It includes effects of single and multiple scattering and whitecap radiance, and is applied only under clear-sky daytime conditions. Major sources of uncertainty in the retrieved water-leaving radiance are: (1) the possibility that the candidate aerosol models may not be representative of some regions; (2) the assumption of zero water-leaving radiance in the two NIR bands may not be valid for regions with high chlorophyll or coccolithophore concentration or turbid water; (3) uncertainty in whitecap radiance; (4) uncertainty in VIIRS out-of-band responses; (5) uncertainty in VIIRS radiometric calibration, polarization sensitivity, and sensor noise. This algorithm produces the VIIRS Remote Sensing Reflectance (RSR) Intermediate Product (IP), which is an input to the VIIRS Ocean Color/Chlorophyll (OCC) unit.

1.0 INTRODUCTION

1.1 PURPOSE

This ATBD describes the algorithm used to produce the VIIRS RSR IP, which consists of the water-leaving reflectance in each of five visible-wavelength VIIRS bands. The RSR IP is used to derive Ocean Color (defined as the Normalized Water-Leaving Radiance) and, with the Carder bio-optics algorithm, to retrieve the remaining VIIRS OCC EDRs (chlorophyll-a concentration and inherent optical properties of absorption and scattering). The algorithm operates on the assumption that the signal in the NIR is due entirely to the atmosphere and the ocean surface, with no in-water contribution. This is a reasonable assumption for non-turbid waters and deep oceans.

1.2 SCOPE

This document covers the algorithm theoretical basis for retrieval of remote sensing reflectance. Section 1 describes the purpose and scope of the document. Section 2 provides an overview of the uses of remote sensing reflectance retrievals and lists relevant VIIRS instrument characteristics. Section 3 describes the algorithm, practical aspects of its operation, results of sensitivity studies, and methods of validation. Section 4 summarizes assumptions and limitations of the algorithm. References for publications cited are given in Section 5.

1.3 VIIRS DOCUMENTS

References to VIIRS documents are indicated by a number in italicized brackets, e.g., *[V-1]*.

[V-1] VIIRS Flowdown Results: Radiometric Noise Requirements for Chlorophyll, RAD.NEDL.OC, 1998.

[Y-2408] VIIRS Algorithm Theoretical Basis Document for Ocean Color, Version 6, August 2005.

[Y-3249] VIIRS Error Budget, Version 3, April 2000. Appendix A of VIIRS Phase I System Verification Report.

[Y-3257] VIIRS Computer Resource Requirements.

1.4 REVISIONS

This is the fifth version of the algorithm theoretical basis document for the atmospheric correction over ocean. The first version of the document was written by Odegard and Vasilkov, dated October 1998. The second version of the document, dated June 1999, was developed through revisions and extensions to the first version by Liu, Odegard, Vasilkov, and Wang. Liu et al. extended the second version to create the third version of this document in May 2000.

The fifth version, written in December 2001, includes updated information on sensor characteristics in Table 1, a new sub-section to address masks and flags, and the spectrally dependent radiance of whitecaps. The changes made for this version (Version 5, December

2002) include the new sub-section 3.3.5 for the sun glint mask. The correction to the instrumental polarization is given in the new sub-section 3.5.2. Stray light and the warning flag for stray light are addressed in the new sub-section 3.5.3. The use of a 3D radiative transfer model to study stray light and using the OMPS UV index for absorbing aerosols are discussed as potential P³I activities.

Revision 6, updated in February 2003, includes modification to the science algorithm in order to make consistent between the science algorithm and this ATBD for initial delivery to the IDPS for Sci2Ops conversion.

Revision 7, updated in August 2005, includes more detail description of the ACO retrieval algorithm, update of model equations, and definition of the RSR IP quality bit and structure.

In January 2008, the VIIRS ACO ATBD, Version 5, Revision 7, dated August 2005 became NGST eMatrix document with document number D43314, initial release.

In February 2008, this ATBD was revised to Revision A with modification to the whitecap correction calculation under the NGST SPCR ALG00001234.

In December 2008, this ATBD was revised to Revision B according to CSR RFS SY_139 under the NGST SPCR ALG00001362.

In May 2010, this ATBD was revised to Revision C with NGAS SPCR ALG00001543 under ECR A-295 for updating the gaseous absorption, polarization correction, and Rayleigh LUT, including a detector-dependent adjustment of the Rayleigh reflectance correction to address detector-to-detector variations of the spectral response function..

2.0 EXPERIMENT OVERVIEW

2.1 OBJECTIVES OF ATMOSPHERIC CORRECTION OVER OCEAN

The goal of atmospheric correction over the ocean is to remove the contributions of scattering in the atmosphere and reflection from the sea surface from the top-of-atmosphere radiances measured by a sensor in the visible region of the electromagnetic spectrum. The quantity retrieved is the normalized water-leaving radiance (nL_w) or Remote Sensing Reflectance (RSR) IP, which is used in the retrieval of the Ocean Color/Chlorophyll EDR. The water-leaving radiance is at most 10 percent of the top-of-atmosphere (TOA) radiance in the visible part of the spectrum (Gordon and Morel, 1983), so accurate atmospheric correction is required. The algorithm is applied under clear-sky daytime conditions for deep-water pixels that are not affected by sun glint. For shallow-water coastal pixels or regions affected by sun glint, the same retrieval algorithm will be applied but the retrievals will be labeled as poor quality.

2.2 INSTRUMENT CHARACTERISTICS

Table 1 lists central wavelengths and bandwidths for the VIIRS visible and NIR bands as well as representative values of TOA radiance above the ocean, L_{typ}. The L_{typ} values match those adopted by MODIS. It is recognized that the SeaWiFS NIR band at 765 is strongly affected by O₂ absorption, which complicates corrections for thin cirrus clouds. To avoid the strong oxygen absorption, the Raytheon VIIRS NIR band is centered at 746 nm with a width of 15 nm.

Table 1. VIIRS Visible and NIR Bands

VIIRS band name	Wavelength (nm)	Bandwidth (nm)	L _{typ} (W m ⁻² μm ⁻¹ sr ⁻¹)
M1	412	20	44.9
M2	445	18	40
M3	488	20	32
M4	555	20	21
M5	672	20	10
M6	746	15	9.6
M7	865	39	6.4

The moderate resolution red band was located at 672 nm with a bandwidth of 20 nm to avoid the water vapor absorption. It can be seen from Figure 1 that the Raytheon band configuration is optimized to reduce the water vapor absorption and to avoid the oxygen absorption. The second NIR band is the heritage SeaWiFS band.

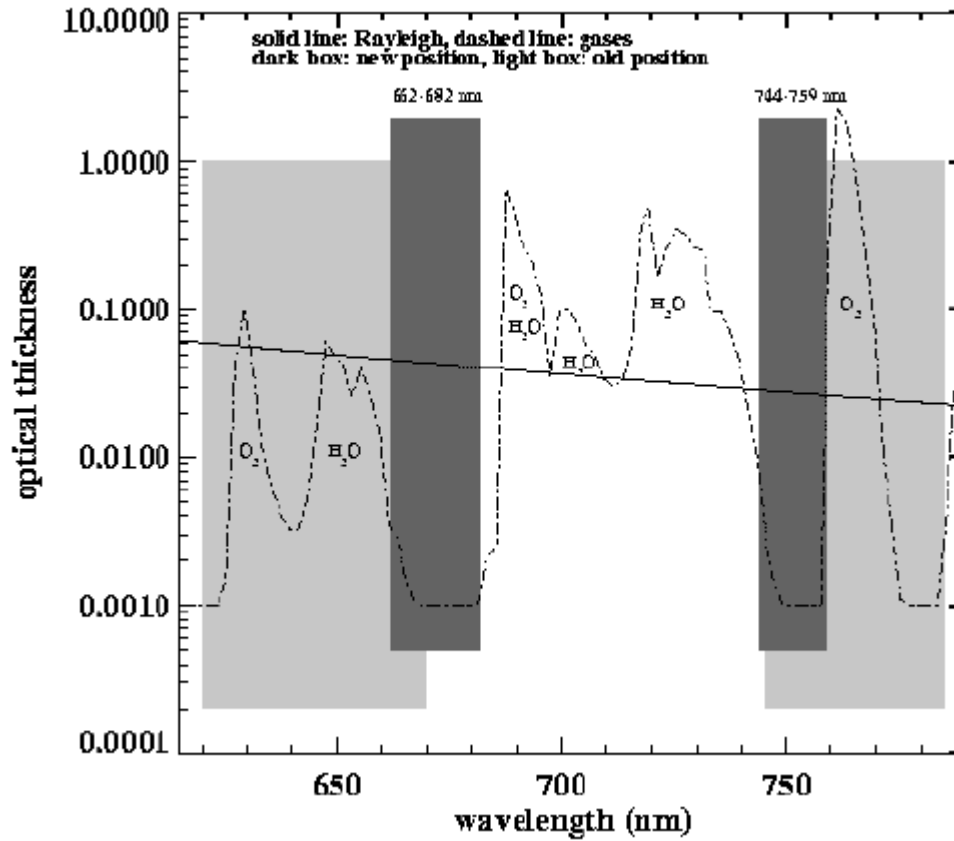


Figure 1. VIIRS band position and width. Solid line represents the Rayleigh optical thickness. The dashed line indicates the optical thickness of gases. In this figure, the right-hand dark box represents the new band centered at 751 nm, which was later adjusted to reduce the influence of the adjacent O₂ absorption feature.

2.3 RETRIEVAL STRATEGY

Atmospheric correction retrievals will be performed only under clear sky, daytime conditions for deep-water regions that have no ice cover and are not affected by sun glint. If a cloud mask, shallow water mask, ice cover mask, or sun glint mask is not set for a given pixel, atmospheric correction of VIIRS top-of-atmosphere radiances is performed. To perform atmospheric correction, non-VIIRS data sets such as surface pressure, total ozone column, total precipitable water, and sea surface wind speed are needed. The output of the atmospheric correction algorithm is the RSR IP, which is an input to the OCC algorithm. Currently, the atmospheric correction over shallow water (depth ≤ 50 m), turbid water, or in sun glint regions is performed with the same deep ocean algorithm but is labeled as poor quality.

3.0 ALGORITHM DESCRIPTION

3.1 PROCESSING OUTLINE

Figure 2 presents a schematic flowchart for the ACO algorithm, which was adapted from Gordon (1996). Processing starts with the TOA radiance measured by the sensor. The radiance L_m measured at the top of the atmosphere in each of the visible to near-infrared bands is multiplied by π and divided by the extraterrestrial solar irradiance, F_0 , and the cosine of the solar zenith angle to obtain the measured reflectance ρ_m . Correction for absorption by atmospheric gases (ozone, water-vapor, and other constant species gases) is applied to obtain the reflectance $\rho_{\text{corr-Gas}}$ in the absence of atmospheric absorption. Next the reflectance contributed by whitecaps is estimated from the surface wind speed W and is subtracted from $\rho_{\text{corr-Gas}}$ to produce $\rho_{\text{corr-WC}}$. On a separate branch of the processing flow, the surface atmospheric pressure P and wind speed W are used with the Rayleigh reflectance and detector-dependent adjustment LUTs to compute the TOA Rayleigh reflectance, ρ_r , and degree of polarization due to Rayleigh scattering, P_r . These are used to generate the polarization corrected Rayleigh reflectance which is subtracted from the residual TOA reflectance after the whitecap correction, $\rho_{\text{corr-WC}}$, producing $\rho_{\text{corr-Ray}}$. The algorithm then goes through a two-step process to correct for the solar glint reflectance, $\rho_{\text{corr-SG}}$, using first an assumed set of aerosol optical thicknesses (AOT) and then an updated set of AOT values retrieved by the aerosol retrieval algorithm to provide the direct transmittance along the solar and sensor paths. Finally, the aerosol reflectance algorithm selects from a family of aerosol models to fit the residual TOA reflectance $\rho_{\text{corr-SG}}$ in the 746 and 865 nm bands, assuming that the water-leaving reflectance in each of these two NIR bands is zero. It interpolates between selected aerosol models to obtain the optimal fit to the residual reflectance at 746 and 865 nm, and to estimate the aerosol reflectance contribution in each of the visible wavelength bands. Upon subtraction of this aerosol reflectance contribution, the TOA water-leaving reflectance is obtained in each of the visible bands. Dividing the TOA L_W by the diffuse atmospheric transmittance along the solar (t_0) and sensor (t) paths gives the RSR IP.

3.2 ALGORITHM INPUT

3.2.1 VIIRS Data

The algorithm uses band-averaged spectral radiance measured at the top of the atmosphere in each of the VIIRS visible and near-infrared bands. These band-averaged radiances can be used because VIIRS is calibrated in radiance units directly.

3.2.2 Non-VIIRS Data

The algorithm takes calibrated reflectance data from the VIIRS SDR, and then uses the total precipitable water, ozone total column, and surface pressure to correct for absorption by atmospheric gases. The surface atmospheric pressure is also used to calculate the Rayleigh optical depth which, together with the near-surface wind speed, is used in computing and correcting for the TOA Rayleigh path reflectance. Finally, the near-surface wind speed and velocity (speed and direction) are used to correct for the whitecap reflectance (Frouin et al., 1996) and to construct a sun glint mask, as well as to compute the sun glint correction for those pixels that are not within the sun glint exclusion region.

3.3 THEORETICAL DESCRIPTION OF ATMOSPHERIC CORRECTION OVER OCEAN RETRIEVALS

3.3.1 Physics of the Problem

The radiance backscattered from the atmosphere and/or sea surface is typically at least an order of magnitude larger than the desired radiance scattered out of the water. The contribution of the water-leaving radiance to the TOA radiance decreases with increasing viewing angle because of the reduction of the diffuse transmittance. The process of retrieving water-leaving radiance from the total radiance measured at the sensor is usually referred to as atmospheric correction, even

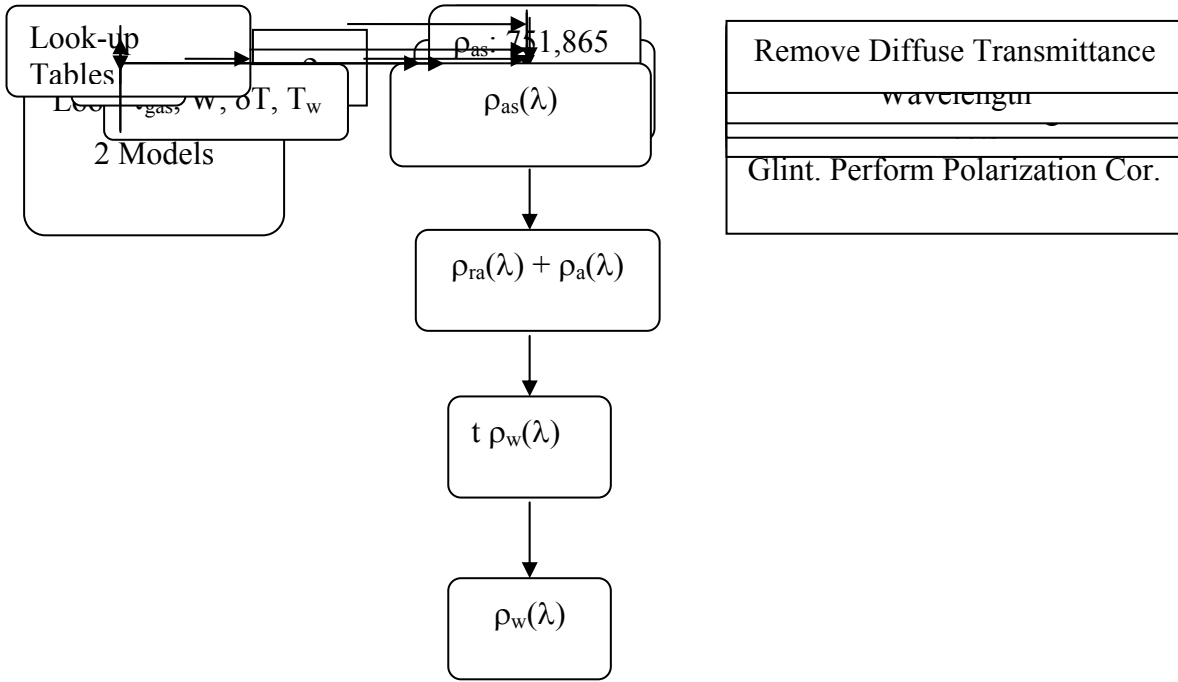


Figure 2. ACO Algorithm flow diagram adapted and modified from Gordon (1996).

though all surface reflection effects other than direct sun glint are removed with a single algorithm. Atmospheric effects are principally due to Rayleigh scattering and scattering by aerosol particles. These effects could be accurately removed if the concentration and optical properties of the aerosol were known. However, these aerosol properties are highly variable in position and time, and the aerosol contribution to the measured radiance at TOA cannot be predicted *a priori*. Therefore, atmospheric correction must be performed for each observation of each pixel, using the measurements themselves to determine the aerosol contribution. A major difficulty of atmospheric correction over the ocean is that the atmospheric and surface radiance contributions to be removed from the top-of-atmosphere radiance are much greater than the water-leaving radiance contribution. It is clear that the atmospheric correction removes a large signal and keeps a very small signal from the water body.

The two NIR bands can be used to derive aerosol information over the ocean since for most water their radiance depends almost entirely on the atmospheric state and the reflection from the air-sea interface. Surface measurements (Herring 1997) show that the water-leaving radiance at NIR bands is usually negligible (see Figure 4). However, it is well known within the ocean color community that for conditions of low aerosol optical thickness and high chlorophyll concentration, the water-leaving radiance in the NIR bands can be significant enough to result in the wrong aerosol types being chosen by the algorithm and a sizeable negative bias being introduced in the retrieved water-leaving radiance. This has also been demonstrated in our recent testing with synthetic data. It should also be pointed out that the ratio of the signal to noise is a key factor affecting the selection of the aerosol model and the calculation of the diffuse transmittance, which converts the water-leaving radiance to the remote sensing reflectance.

3.3.2 Mathematical Description of the Algorithm

The upward radiance at the top of the atmosphere over the ocean is composed of the atmosphere-scattered radiance, air-sea interface reflected radiance, and transmitted water-leaving radiance (see Figure 5). The VIIRS ACO algorithm is described in detail by Gordon et al. (1996) and Gordon (1997a); only a summary is presented here.

The upward unpolarized radiance at the top-of-atmosphere (TOA), $L_{TOA}(\lambda)$, can be written as:

$$L_{TOA}(\lambda) = L_{path}(\lambda) + T(\theta_v, \lambda) L_g(\lambda) + t(\theta_v, \lambda) L_{wc}(\lambda) + t(\theta_v, \lambda) L_w(\lambda) \quad (1)$$

Here L_{path} is the radiance originating along the optical path from scattering in the atmosphere and from specular reflection of scattered light (skylight) by the sea surface, L_g is the radiance originating from specular reflection of direct sunlight by the sea surface (sun glitter), L_{wc} is the radiance originating from reflection of direct sunlight and skylight from whitecaps, and L_w is the water-leaving radiance from whitecap-free areas of the surface. $T(\theta_v)$ and $t(\theta_v)$ are the direct transmittance and the diffuse transmittance, respectively, of the atmosphere along the path from the ocean surface to the sensor. λ are the VIIRS wave bands and θ_v are the sensor zenith angles. The path radiance can be decomposed into three components:

$$L_{path}(\lambda) = L_r(\lambda) + L_a(\lambda) + L_{ra}(\lambda) \quad (2)$$

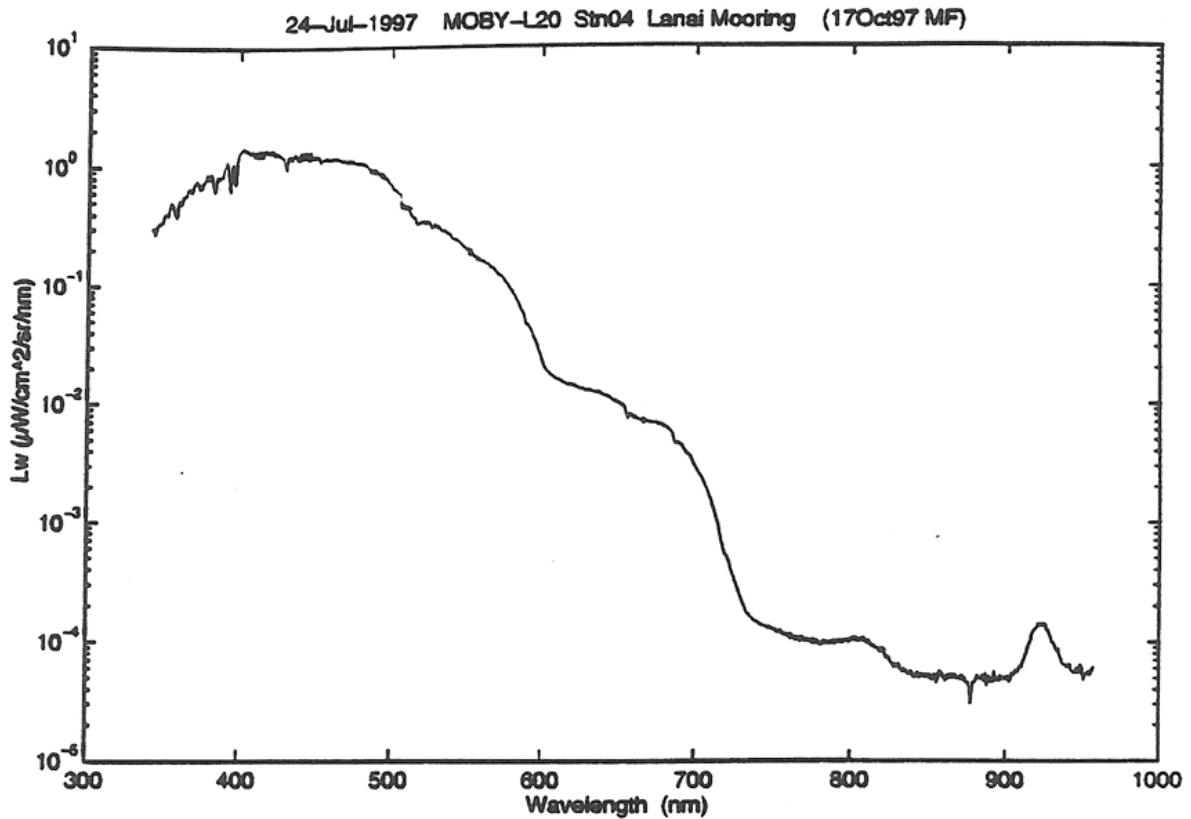


Figure 4. Spectral variation of the water-leaving radiances measured by the high-resolution spectrographs on MOBY.

where L_r is the radiance originating from single and multiple scattering by air molecules (Rayleigh scattering), L_a is the radiance originating from single and multiple scattering by aerosols, and L_{ra} is the radiance originating from multiple scattering events involving both Rayleigh and aerosol scattering.

The above representation for the TOA radiance assumes that the sensor is completely insensitive to the polarization state of the radiation at TOA. However, all sensors have some polarization sensitivity, and since the radiation measured at TOA is generally polarized, the radiance actually measured by the sensor, L_m , will have additional terms that represent the bias in the radiance introduced by the degree of polarization in the TOA radiation and the sensor polarization sensitivity. To derive an expression for L_m , we follow the development in Section 3.4.4. Starting with Equation (11) and replacing the total intensity of the Stokes vector, I , with L , we have that:

$$L_m = L_{TOA} [1 + P_{in} P \cos 2(\alpha - \varphi - \chi_{in})],$$

where,

P_{in} = Instrument polarization sensitivity

χ_{in} = Instrument polarization phase angle

$$P = \text{Degree of polarization at TOA} \equiv \frac{\sqrt{Q_{TOA}^2 + U_{TOA}^2}}{L_{TOA}}$$

$$\varphi = \text{Polarization phase angle at TOA} \equiv \frac{1}{2} \tan^{-1} \left(\frac{U_{TOA}}{Q_{TOA}} \right)$$

Replacing the expression for P in the above equation, we can rewrite it as,

$$L_m = L_{TOA} + P_{in} \sqrt{Q_{TOA}^2 + U_{TOA}^2} \cos 2(\alpha - \varphi - \chi_{in}).$$

Then combining Equations (1) and (2) for L_{TOA} and noting that essentially all of the polarization in the TOA radiation is due to Rayleigh scattering, we obtain,

$$L_m = L_r(\lambda) + L_a(\lambda) + L_{ra}(\lambda) + T(\theta_V, \lambda) L_g(\lambda) + t(\theta_V, \lambda) L_{WC}(\lambda) + t(\theta_V, \lambda) L_W(\lambda) + P_{in} \frac{\sqrt{Q_r^2 + U_r^2}}{L_r} L_r \cos 2(\alpha - \varphi - \chi_{in}),$$

or

$$L_m = L_r(\lambda) [1 + P_{in} P_r \cos 2(\alpha - \varphi - \chi_{in})] + L_a(\lambda) + L_{ra}(\lambda) + T(\theta_V, \lambda) L_g(\lambda) + t(\theta_V, \lambda) L_{WC}(\lambda) + t(\theta_V, \lambda) L_W(\lambda)$$

Defining the Rayleigh polarization correction, PolCor, as $[1 + P_{in} P_r \cos 2(\alpha - \varphi - \chi_{in})]$ and converting from radiance L to reflectance ρ using the definition $\rho \equiv \pi L / (F_0 \cos \theta_0)$, where F_0 is the extraterrestrial solar irradiance and θ_0 is the solar zenith angle, yields:

$$\rho_m(\lambda) = \rho_r(\lambda) * \text{PolCor} + \rho_a(\lambda) + \rho_{ra}(\lambda) + T(\theta_V, \lambda) \rho_g(\lambda) + t(\theta_V, \lambda) \rho_{WC}(\lambda) + t(\theta_V, \lambda) \rho_W(\lambda)$$

The final thing to note in the above equation is that it does not include the effect of absorption by atmospheric gases. In order to treat atmospheric absorption rigorously, one would need to look at the individual terms to see how they are each affected by the different gases and their location in the atmosphere. However, since the ocean color bands are well centered in the window regions of the atmosphere, where atmospheric absorption is small, we can with good accuracy include the effects of atmospheric absorption by dividing the measured reflectance ρ_m by the gaseous direct transmittance along the solar and sensor paths, $T_{gas-sol}$ and $T_{gas-sens}$ respectively.

The goal of the atmospheric correction algorithm is to retrieve the water-leaving reflectance ρ_w in each of the VIIRS visible wavelength bands. A sun glint mask is used to flag data for viewing geometries where the sun glint contribution is significant. The mask is constructed based on ancillary wind velocity data and the Cox-Munk (1954) model for the roughness slope statistics of the wind-ruffled sea surface.

A brief description of the processing steps of the atmospheric correction algorithm was provided in Section 3.1. In short, the correction steps can be summarized as:

$$t\rho_w = \left[\frac{\rho_m(\lambda)}{T_{gas-sol}(\lambda)T_{gas-sen}(\lambda)} - t(\theta_V, \lambda)\rho_{WC}(\lambda) - \rho_r * PolCor - T(\theta_V, \lambda)\rho_g(\lambda) - \rho_a(\lambda) - \rho_{ra}(\lambda) \right] \quad (3)$$

The two-way gaseous transmittance for each ocean band is given as the product of the direct transmittances due to ozone, water-vapor and other constant species gases (O_2 , CO_2 , CO , CH_4 , and NO_X); that is, $T_{gas} = T_{oz} T_{h2o} T_{og}$. Following the development in 6S(V), simple expressions for these band-averaged transmittances are legislated as a function of the two-way air mass, the total column amount of gas (used for ozone and water-vapor), and the surface pressure (used for constant species gases). The functional form of the transmittance used for each gas is provided below.

The two-way ozone transmittance for each ocean band is given as

$$T_{oz}(\lambda) = e^{-Z \cdot k_{oz}(\lambda) \left(\frac{1}{\mu} + \frac{1}{\mu_0} \right)}$$

where, Z is the total column ozone concentration in atmospheres-cm (converted from Dobson by dividing by 1000), $k_{oz}(\lambda)$ is the ozone absorption coefficient, μ is the cosine of the viewing zenith angle, μ_0 is cosine of the solar zenith angle. The two-way water vapor transmittance for each ocean band is given as

$$T_{H2O}(\lambda) = e^{a(\lambda) \cdot x + b(\lambda) \cdot \log(x) + c(\lambda) \cdot x \cdot \log(x)}$$

$$x = U \left[\frac{1}{\mu} + \frac{1}{\mu_0} \right]$$

Where, U is the total precipitable water, a , b , and c are the band dependent water vapor absorption coefficients. The two-way transmittance for other constant species gases is given as:

$$T_{OG}(\lambda) = \exp[m \cdot (a_0 P + a_1 \log P)] \cdot \exp[(b_0 P + b_1 \log P) \cdot \log(m)] \cdot \exp[(c_0 P + c_1 \log P) \cdot m \log(m)]$$

$$m = \frac{1}{\mu} + \frac{1}{\mu_0}$$

where P is the surface pressure, a_0 , a_1 , b_0 , b_1 , c_0 , and c_1 are the band dependent absorption coefficients.

The coefficients in the above expressions for gaseous transmittance were fit using a regression algorithm with a matchup dataset of band-averaged transmittances (computed with 6SV for the 6 US Standard Atmospheres and a range of solar and sensor zenith angles) and their associated values for the two-way air mass, total column amount of gas, and surface pressure. The resulting total gaseous transmittance along the solar and sensor paths are then used to compute the gaseous

absorption corrected reflectance $\rho_{\text{corr-Gas}}(\lambda)$ as
$$\frac{\rho_m(\lambda)}{T_{\text{gas-sol}}(\lambda)T_{\text{gas-sen}}(\lambda)}$$

The whitecap contribution for each ocean band is small and is calculated as a function of wind speed and viewing geometry using the equation according to SeaDAS version 5.1:

$$\rho_{\text{wc}}(\lambda) = 0.4 * 6.49 * 10^{-7} * W^{3.52} * f_{\text{wc}}(\lambda) \quad (4)$$

where

$$f_{\text{wc}}(\lambda) = a_{\text{wc}}(\lambda) \cdot t_{\text{sat}} \cdot t_{\text{sol}}$$

with $a_{\text{wc}}(\lambda) = 1.0$ at M1 to M4, $a_{\text{wc}}(M5) = 0.889225$, $a_{\text{wc}}(M6) = 0.760046$, $a_{\text{wc}}(M7) = 0.644950$, W is the non-zero windspeed (m/s), t_{sat} and t_{sol} are the diffuse transmittance along the viewing and solar paths respectively due to Rayleigh and aerosol scattering. The spectral-dependence of the reflectance due to whitecaps is adopted from the work of Frouin et al. (1996), and is given above in the $a_{\text{wc}}(\lambda)$ terms. Like the current MODIS processing, the whitecap reflection is capped off at a surface wind speed of 8 m/s.

The Rayleigh scattering contribution ρ_r can be calculated accurately, including polarization effects, from ancillary surface atmospheric pressure and wind speed data (Gordon et al., 1988; Gordon and Wang, 1992; Wang, 2002). The Rayleigh radiance for each of the ocean bands is given by:

$$L_{\text{rayleigh}}(\lambda) = G(\lambda) \cdot \left(\frac{1 - e^{-c\tau_r(\lambda) \frac{P}{P_0} \left(\frac{1}{\mu} + \frac{1}{\mu_0} \right)}}{1 - e^{-c\tau_r(\lambda) \left(\frac{1}{\mu} + \frac{1}{\mu_0} \right)}} \right)$$

where $G(\lambda)$ is the multiple scattering Rayleigh coefficient interpolated from the Rayleigh scatter polarization LUT for each band, $\tau_r(\lambda)$ is the Rayleigh optical depth for each band, P is pressure, and P_0 is standard surface pressure, and c is a factor to account for the atmospheric pressure variation,

$$c = -(0.6543 - 1.608 \cdot \tau_r) + (0.8192 - 1.2541 \cdot \tau_r) \log \left(\frac{1}{\mu} + \frac{1}{\mu_0} \right).$$

With the improved knowledge of the relative spectral response (RSR) for VIIRS bands M1-M7 obtained from final sensor characterization, the Rayleigh LUT used by the ACO code has recently been updated, as described in the OAD.

Upon examination of the individual detector RSRs obtained for each band, it was determined that there is sufficient detector-to-detector variation (especially for band M1) to warrant implementing a simple detector-dependent adjustment to the TOA Rayleigh radiance correction determined from the Rayleigh LUT, which is based solely on detector-averaged RSRs. The detector-dependent adjustment multiplies the normalized radiance obtained from the Rayleigh Radiance LUT by the ratio of the band-averaged Rayleigh Optical Thickness computed from each detector RSR to that produced from the detector-averaged RSR. This approach is based on the approximation for the band-averaged Rayleigh radiance from Gordon [2], where:

$$\langle L_r(\lambda) \rangle_{S_i} \cong G(\theta_0, \theta_V, \phi) \int_{\lambda} \tau_r(\lambda) F_0(\lambda) S_i(\lambda) d\lambda$$

$$\text{so that } \langle \widehat{L}_r(\lambda) \rangle_{S_i} \equiv \frac{\langle L_r(\lambda) \rangle_{S_i}}{\langle F_0(\lambda) \rangle_{S_i}} \cong G(\theta_0, \theta_V, \phi) \frac{\int_{\lambda} \tau_r(\lambda) F_0(\lambda) S_i(\lambda) d\lambda}{\int_{\lambda} F_0(\lambda) S_i(\lambda) d\lambda} = G(\theta_0, \theta_V, \phi) \langle \tau_r(\lambda) \rangle_{S_i}$$

Based on the above relation, the normalized band-averaged Rayleigh radiance for each detector, $\langle \widehat{L}_r(\lambda) \rangle_{S-Det}$, can be easily determined using the normalized band-averaged radiance from the Rayleigh LUT, $\langle \widehat{L}_r(\lambda) \rangle_{S-Avg}$ and the ratio of the Rayleigh Optical Thicknesses; that is,

$$\langle \widehat{L}_r(\lambda) \rangle_{S-Det} = \langle \widehat{L}_r(\lambda) \rangle_{S-Avg} \frac{\langle \tau_r(\lambda) \rangle_{S-Det}}{\langle \tau_r(\lambda) \rangle_{S-Avg}}$$

The above ratio of Rayleigh Optical Thicknesses has been pre-computed for each detector and is provided as a detector-dependent Rayleigh correction factor LUT, as described in the OAD.

In terms of the sequence in computing the Rayleigh atmospheric correction, the nominal Rayleigh contribution based on the detector-averaged RSR is computed from the Rayleigh LUT with given solar and sensor geometry, wind speed, surface pressure, and AOT. Then the detector-dependent adjustment to the Rayleigh correction is made using the LUT of pre-computed detector-dependent Rayleigh reflectance adjustment factors.

The derivation of the instrument polarization correction, PolCor, applied with the Rayleigh reflectance $\rho_r(\lambda)$ at each ocean band was described in Section 3.3.2. Briefly, the polarization correction is given as $PolCor = [1 + P_{in} P_r \cos 2(\alpha - \varphi - \chi_{in})]$, where P_{in} and χ_{in} are the instrument polarization sensitivity and polarization phase angle respectively, P_r and φ are the TOA degree of linear polarization due just to Rayleigh scattering, and α specifies the rotation angle between the coordinate system in which the calculation is performed and the coordinate system of the instrument. For VIIRS F1, this angle is zero. The polarization correction and the correction for the Rayleigh reflectance are made simultaneously by subtracting the product of $\rho_r * PolCor$ from the TOA measured reflectance.

The details of the aerosol correction are described in Gordon (1997a), Gordon and Voss (1999), and Wang (2004). The contribution involving aerosol scattering, $\rho_A \equiv \rho_a + \rho_{ra}$, cannot be determined accurately from available ancillary data. Its magnitude and wavelength dependence

can vary greatly with position and time, due to variations in aerosol concentration and aerosol optical properties. The Gordon-Wang algorithm makes the assumption that $\rho_w = 0$ in the two VIIRS NIR bands (751 and 865 nm), so the aerosol contribution in these bands is given by $\rho_A = \rho_m - \rho_r - t \rho_{wc}$. The algorithm then selects from a family of 12 aerosol models to fit the aerosol contribution in the NIR bands and to estimate the aerosol contribution in the visible bands. The 12 aerosol models are the same models currently used for SeaWiFS and MODIS processing. They are listed in Table 2. The Oceanic, Maritime, and tropospheric aerosol models are from Shettle and Fenn (1979), while the coastal aerosol model is introduced by Gordon and Wang (1994a), consists of 99.5 percent tropospheric aerosols and 0.5 percent oceanic aerosols. The tropospheric and oceanic components of these models are specified by particle size distributions and refractive indices that vary as a function of relative humidity. The algorithm makes use of Mie theory to calculate look-up tables for each aerosol model, giving $\rho_A(\lambda)$ for different relative humidity values, different aerosol concentrations, and different solar and viewing geometries. The radiative transfer calculations are done for a two-layer plane parallel atmosphere bounded by a smooth Fresnel-reflecting ocean surface, with all aerosol scattering occurring in the lower layer and all Rayleigh scattering occurring in the upper layer. Effects of multiple scattering and polarization effects are included. The different aerosol models used are thought to be representative of aerosols present over the oceans; none of the models are appropriate for strongly absorbing aerosols such as desert dust or urban pollution. For future improvement, algorithms are currently being explored that could incorporate bands M8 and M10 to improve correction for aerosols.

Table 2. The 12 aerosol models used in the VIIRS ACO algorithm

Number	Aerosol Model	Description
1	O99	Oceanic with relative humidity of 99%
2	M50	Maritime with relative humidity of 50%
3	M70	Maritime with relative humidity of 70%
4	M90	Maritime with relative humidity of 90%
5	M99	Maritime with relative humidity of 99%
6	C50	Coastal with relative humidity of 50%
7	C70	Coastal with relative humidity of 70%
8	C90	Coastal with relative humidity of 90%
9	C99	Coastal with relative humidity of 99%
10	T50	Tropospheric with relative humidity of 50%
11	T90	Tropospheric with relative humidity of 90%

12	T99	Tropospheric with relative humidity of 99%
----	-----	--

After subtraction of the whitecap, Rayleigh, and aerosol contributions from ρ_m , division by the diffuse transmittance is required to obtain water-leaving reflectance ρ_w . For a general atmosphere composed of both air molecules and aerosols bounded by a Fresnel-reflecting ocean surface, the diffuse transmittance is given approximately by $t(\lambda, \theta) = t_r(\lambda, \theta) \cdot t_a(\lambda, \theta)$ (Gordon and Voss, 1999; Wang, 1999), where

$$t_r(\lambda, \theta) \approx \exp[-C_r(\lambda, \theta)\tau_r(\lambda)/2 \cos \theta]$$

$$t_a(\lambda, \theta) \approx \exp\{-a_0(\lambda)[1 + \omega_a(\lambda)C_a(\lambda, \theta)]/\cos \theta\}$$

$$a_0(\lambda) = [1 - \omega_a(\lambda)F_a(\lambda)]\tau_a(\lambda)$$

$$F_a(\lambda) = \frac{1}{2} \int_0^1 P_a(\Theta, \lambda) d\cos \Theta$$

in which $\tau_r(\lambda)$ and $\tau_a(\lambda)$ are the Rayleigh optical thickness (molecular scattering) and aerosol optical thickness respectively, $\omega_a(\lambda)$ are the aerosol single scattering albedo, $C_r(\lambda, \theta)$ and $C_a(\lambda, \theta)$ are fitted parameters. The diffuse transmittance LUT employed by the ACO code is based on a simpler exponential approximation (Yang and Gordon, 1997):

$$t(\lambda, \theta) = A(\theta)\exp[-B(\theta)\tau_a(\lambda)], \quad (5)$$

where $A(\theta)$ and $B(\theta)$ are pre-computed parameters in the LUT for each of the twelve aerosol models. Diffuse transmittance can therefore be approximated using Equation (5). These are discussed in Gordon et al. (1983) and Wang (1999).

The algorithms that have been adopted for retrieval of the VIIRS Ocean Color/Chlorophyll EDR make use of remote-sensing reflectance IP R_{rs} , the ratio of water-leaving radiance to downwelling irradiance just above the sea surface. R_{rs} values can be determined from:

$$R_{rs}(\lambda) = \rho_w(\lambda)/[\pi t(\theta_0, \lambda)] \quad (6)$$

3.3.3 Diffuse Transmittance

As described in the above section, the diffuse transmittance is computed through LUT for a given aerosol model, aerosol optical thickness, and solar or sensor zenith angle for the VIIRS seven ocean color bands. The diffuse transmittance tables were generated using the vector radiative transfer (including polarization) for the two-layer atmosphere (aerosols at the bottom mixed with 22% of molecules) bounded by a flat Fresnel reflecting ocean surface. The table coefficients $A(\theta)$ and $B(\theta)$ were generated as described in Yang and Gordon (1997), i.e., Equation (5). The lookup tables were generated for the 12 aerosol models that are currently used for the SeaWiFS and MODIS data processing. They are given in Table 2. The lookup tables are for the solar or sensor zenith angles varying from 0 up to 80 (degree).

3.3.4 Aerosol effect

The Rayleigh scattering effect can be easily removed because its phase function is a well-known analytic function and its optical thickness can be calculated according to the surface pressure. The aerosol effect, however, is a more uncertain component of the atmospheric correction. Different aerosols have different behavior, especially absorbing aerosols. The particle size of aerosol grows with increasing relative humidity. It can be seen from Figure 7a that the phase function of aerosols depends on the aerosol type as well as the relative humidity. The single scattering approach is the basis of the present method for selecting aerosol models; it is a good approximation because of the low optical thickness of the aerosols over the ocean. The single scattering effect for small optical thickness is a product of the single scattering albedo, phase function, and optical thickness. It is known that the ratio of this product at two wavelengths is approximately an exponential function (see Figure 7b). In principle, radiances at the two NIR bands can determine one straight line in the epsilon-wavelength plane, where epsilon $\epsilon(751,865)$ is defined as the 751 nm over 865 nm band ratio of single scattering aerosol reflectance. However, sensor noise and algorithm error could prevent a correct selection of the aerosol model. Therefore, radiometric noise is an issue for the atmospheric correction over ocean. The combination of the red band at 672 nm and the NIR band at 865 nm may have an advantage for the atmospheric correction in some cases because of the large difference between the wavelengths of the two bands.

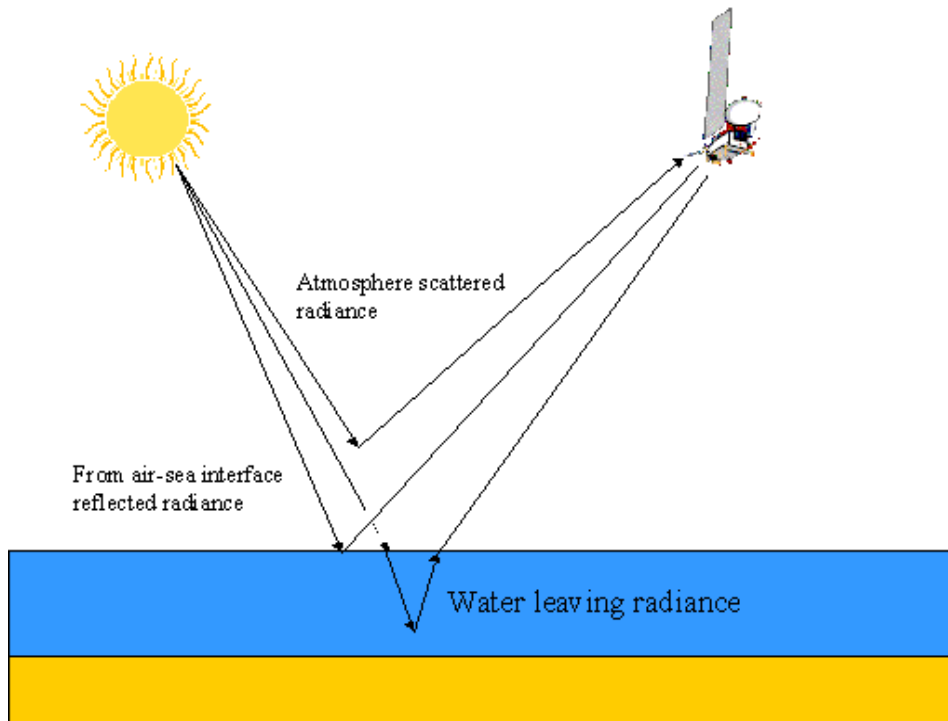


Figure 5. Schematic drawing of the radiation transport.

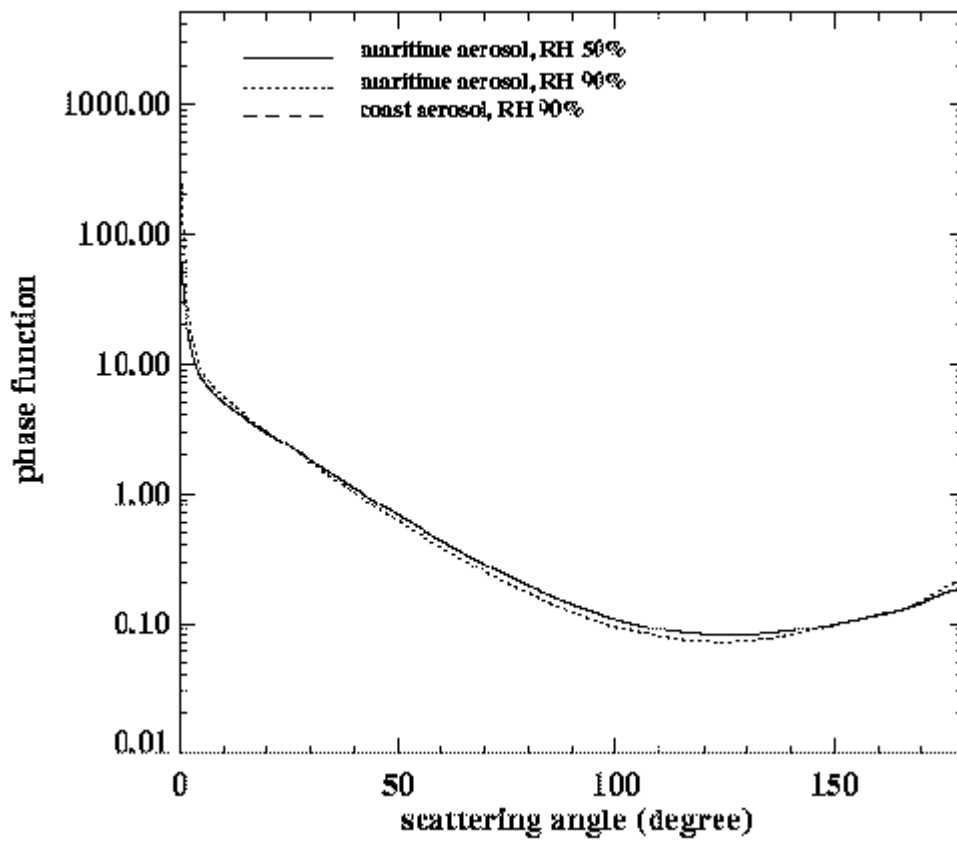


Figure 7a. Variation of the phase function with the scattering angle.

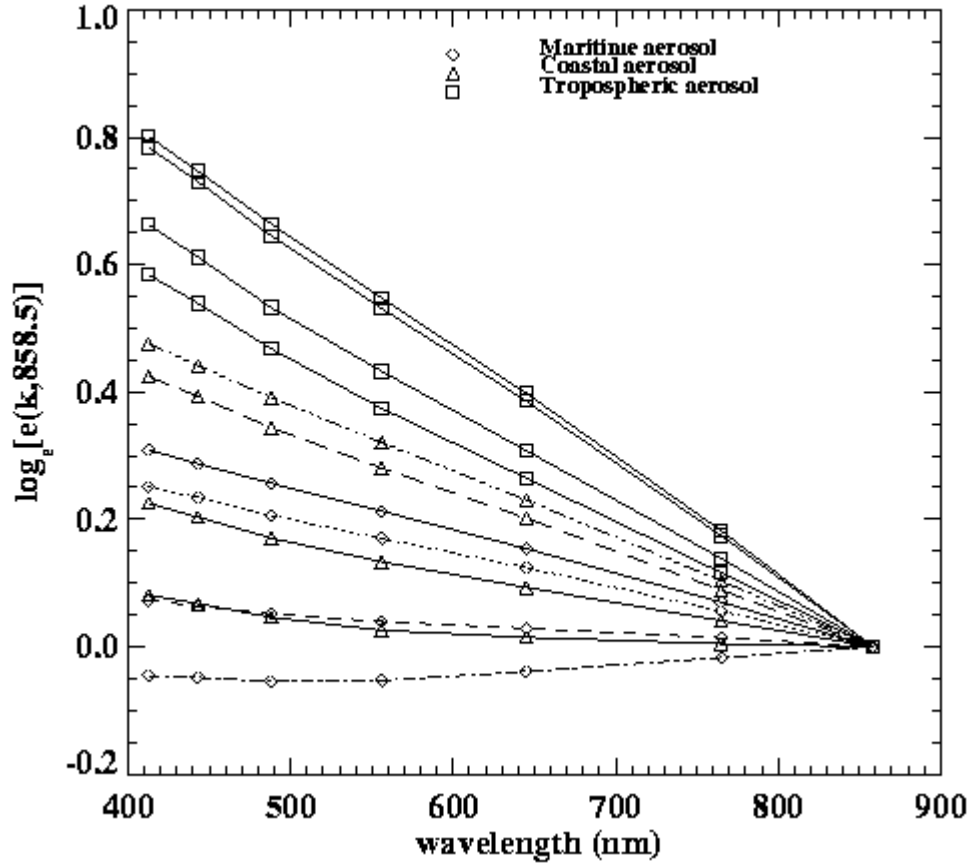


Figure 7b. Values of $\epsilon(\lambda, 858)$ for nadir viewing with $\theta_0=60^\circ$ for the maritime, costal, and tropospheric aerosol models. For each model, the relative humidity values are 50, 70, 90, and 99% from the top to the bottom curves.

3.3.5 Sun glint mask and correction

Sun glint refers to the phenomenon of incoming solar radiation directly reflected from the ocean surface to the sensor. For an absolutely flat ocean surface, the sun glint occurs at one point where the zenith angles of sun and sensor are identical and their azimuth angles are opposite. However, the ocean surface is never absolutely flat. The wind-derived surface roughness enlarges the sun glint area (see Figure 8).

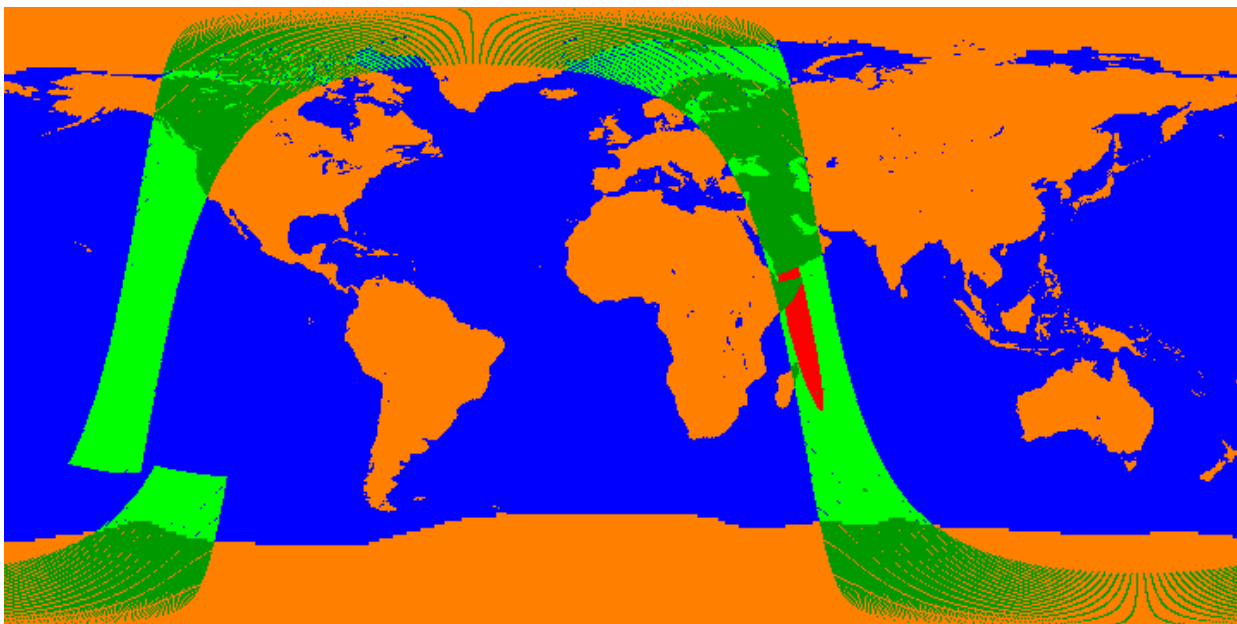


Figure 8. Sun glint (red color) area for a wind speed of 8 m s^{-1} for simulated 1330 VIIRS orbit.

In the science code, sun glint information is expected to come from the VIIRS cloud mask. In addition, we adopt the same sun glint correction technique that is currently used in the SeaDAS software for both SeaWiFS and MODIS processing. Retrieval is performed under sun glint regions but is indicated as poor quality in the quality flag.

3.3.6 Algorithm Output

Outputs of the algorithm to be used for EDR processing are the remote-sensing reflectance R_{rs} in the VIIRS 412, 445, 488, 555, and 672 nm bands, the aerosol optical depth at 865 nm, and quality flags listed in Table 2 (a) and (b).

Table 2 (a). Bit Structure of the Pixel Level Quality Flags for the RSR IP

BYTE	Bit	Flag Description Key	Bit Value
0	0	RSR quality at M1	0 = Good, 1 = Poor
	1	RSR quality at M2	0 = Good, 1 = Poor
	2	RSR quality at M3	0 = Good, 1 = Poor
	3	RSR quality at M4	0 = Good, 1 = Poor
	4	RSR quality at M5	0 = Good, 1 = Poor
	5	$L_{aer}(M6) \leq 1.1$	0 = Yes ($L_{aer}(M6) \leq 1.1$) 1 = No, or no $L_{aer}(M6)$ available
	6	Spare	Set to 0
	7	Spare	Set to 0
1	0	SDR Quality for Ocean Bands M1 to M7	0 = Good for all 7 bands 1 = Poor (any band greater than thresholds)
	1	Input Total Ozone Column Quality	0 = Good, 1 = Poor
	2	Wind Speed Indicator	0 = Low wind ($0 \leq \text{speed} \leq 8.0$ m/s) 1 = High wind (speed > 8.0 m/s)
	3	Epsilon Out of Aerosol Models Range	0 = Within model range ($0.85 \leq \epsilon \leq 1.35$) 1 = Out of model range, or no ϵ available
	4-6	Atmospheric Correction Failure	000 = Atmospheric correction successful 001 = Ozone correction failure 010 = Whitecap correction failure 011 = Polarization correction failure 100 = Rayleigh correction failure 101 = Aerosol correction failure 110 = Zero diffuse transmittance 111 = No correction possible
	7	Spare	Set to 0
2	0-1	Land/water	00 = Sea water, 01 = Coastal water, 10 = Inland water, 11 = Land
	2	Snow/Ice	0 = Not snow/ice 1 = Snow/ice
	3	Day/Night Exclusion	0 = Day ($SZA \leq 70^\circ$) 1 = Night ($SZA > 70^\circ$) exclusion
	4	Sun Glint Exclusion	0 = No sun glint, 1 = Sun glint
	5	Horizontal Reporting Interval (HRI) > 1.3 km Exclusion	0 = No, Nadir to 1.3 km ($0^\circ \leq \text{Sensor Zenith Angle} \leq 50.3^\circ$) 1 = Yes, HRI > 1.3 km exclusion
	6	Shallow Water	0 = Deep water (Depth ≥ 50 m) 1 = Shallow water (Depth < 50 m)
	7	Stray Light Maximum Radiance Exclusion	0 = No exclusion, or no mask available 1 = Stray light exclusion
3	0-1	Cloud Confident Indicator	00 = Confident clear, 01 = Probably clear 10 = Probably cloudy, 11 = Confident cloudy
	2	Adjacent Pixel Cloud Confident Indicator	0 = Confident clear, 1 = Cloudy

BYTE	Bit	Flag Description Key	Bit Value
	3	Cirrus Cloud Detection	0 = No Cirrus detected 1 = Cirrus detected
	4	Cloud Shadow Exclusion	0 = No cloud shadow, 1 = Shadow present
	5	Non Cloud Obstruction (Heavy Aerosol)	0 = No, 1 = Yes
	6	Strongly Absorbing Aerosol (Single Scattering Albedo $\omega_0(M4) < 0.7$) Exclusion	0 = No exclusion, or no $\omega_0(M4)$ available 1 = Strongly absorbing aerosol present ($\omega_0(M4) < 0.7$)
	7	Aerosol Optical Thickness (AOT @ M7) Exclusion (AOT > 1.0)	0 = No AOT exclusion, or no AOT available 1 = AOT exclusion (AOT > 1.0)

Table 2 (b). Granule Level Quality Flags for the RSR IP

Input	Type	Description/Source	Units/Range
Overall RSR IP Quality at M1	Integer	Percent of high quality Ocean Color retrievals at M1 / Ocean Color/Chlorophyll EDR	0 % to 100 %
Overall RSR IP Quality at M2	Integer	Percent of high quality Ocean Color retrievals at M2 / Ocean Color/Chlorophyll EDR	0 % to 100 %
Overall RSR IP Quality at M3	Integer	Percent of high quality Ocean Color retrievals at M3 / Ocean Color/Chlorophyll EDR	0 % to 100 %
Overall RSR IP Quality at M4	Integer	Percent of high quality Ocean Color retrievals at M4 / Ocean Color/Chlorophyll EDR	0 % to 100 %
Overall RSR IP Quality at M5	Integer	Percent of high quality Ocean Color retrievals at M5 / Ocean Color/Chlorophyll EDR	0 % to 100 %
Input SDR Quality	Integer	Percent of high quality VIIRS SDR data input / VIIRS SDR	0 % to 100 %
No Day Pixel in Granule	Integer	Indicates whether any day pixels are in the current granule / Solar zenith angles	0 = Day pixels in granule 1 = No day pixels in granule
Exclusion Summary	Integer	Percent of pixels have one or more exclusion conditions	0 % to 100 %
No Ocean Coverage	Integer	Granule No Ocean flag / VIIRS Cloud Mask IP	0 = Ocean 1 = No ocean

3.3.7 Variance and Uncertainty Estimates

Estimates of the variance and uncertainty of the retrieved water-leaving radiance were presented by Gordon (1997a) for different sources of error. Below we briefly review error estimates for these sources of uncertainty.

Multiple scattering effects may be significant at the level of accuracy required for VIIRS. Although the single scattering approach works well for sufficiently small optical thickness, typically the case over the open ocean, it is desirable to consider extreme situations. The influence of multiple scattering depends significantly on the aerosol model. For example, for the maritime aerosol model, multiple scattering increases atmospheric reflectance by about 40

percent in comparison to single scattering. Multiple scattering effects are accounted for using look-up tables for twelve candidate aerosol models. Testing shows that the multiple-scattering algorithm retrieves water-leaving reflectance at 445 nm with uncertainty less than 0.002 for non-absorbing aerosol models.

The impact of aerosol absorption on multiple scattering may be strong. To account for the aerosol absorption effect, it is important that the relationship between particle size and absorption is approximately correct for each of the candidate aerosol models. Such a relationship must be based on climatology, e.g., when the aerosol optical thickness over the North Atlantic Saharan dust zone is high, we will use candidate models consisting of a linear combination of a maritime model and Saharan dust model.

Whitecaps have the potential of producing errors of a magnitude similar to the magnitude of the acceptable error. Measurements have shown that whitecaps may reflect considerably less in the NIR than in the visible, presumably because a significant component of the whitecap reflectivity is due to scattering from submerged bubbles. The possible spectral dependence of the whitecap reflectivity is directly transposed onto the water-leaving radiance spectrum, thus resulting in errors in chlorophyll concentrations derived from band ratio algorithms. If the error in the estimate of whitecap reflectivity at 445 nm is ± 0.002 , the error in the normalized water-leaving reflectance may range from approximately +0.0015, to -0.0025.

Aerosol vertical structure may affect the multiple scattering. Studies (Gordon, 1997a; Gordon and Voss, 1999) of this effect have shown that as long as the aerosol is weakly absorbing ($\omega_a > 0.93$), the error is negligible, but as ω_a decreases, the error becomes progressively larger. For example, the algorithm can tolerate only a ± 1 km error in the aerosol layer thickness for lookup tables calculated for the urban candidate model with physical thickness of 2 km.

In calculations of lookup tables for aerosol multiple scattering, polarization effects were considered (Wang 2002). Preliminary computation of polarization effects showed that possible uncertainty in water-leaving reflectance at 445 nm was acceptable, i.e., typically less than 0.001. Thus, compared to the errors possible when strongly absorbing aerosols or whitecaps are present, this error appears negligible.

Simulation showed that ignoring the surface roughness in computation of the lookup tables relating multiple scattering to single scattering reflectance values does not appear to lead to significant error (Gordon and Wang, 1992).

3.4 ALGORITHM SENSITIVITY STUDIES

3.4.1 Calibration Errors

In a Raytheon ITSS study, a 1.5% calibration error may result in a 10 – 15% error for the accuracy of the remote-sensing reflectance. The calibration accuracy requirement for the atmospheric correction is therefore very high. It is because the atmospheric correction extracts the small water-leaving radiance from the TOA radiance. To achieve 10% accuracy at the green band, a calibration accuracy of 0.5% is required, where perfect atmospheric correction is assumed. Such a high accuracy for the onboard radiometric calibration is thought to be beyond the capabilities of current sensors. Therefore, vicarious calibration of the sensor for ocean color is required (See Section 3.6.3).

3.4.2 Instrument Noise

The threshold requirement for chlorophyll measurement precision was 20 percent and the threshold measurement range is 0.05 to 50 mg/m³. According to the Raytheon ITSS estimates, the resultant specification on the chlorophyll precision requirement imposes the maximum allowed radiometric noise in the VIIRS sensor specifications for the VIIRS visible wavelength bands. We have used simulations of TOA radiances over the ocean to assess the effects of sensor noise in the visible and near-infrared VIIRS bands on the precision of chlorophyll retrievals, for each of the different VIIRS sensor performance models developed by Hucks (1998). The effects of noise in the visible bands and in the near-infrared bands were considered independently. In aerosol correction, the ACO algorithm selects the two aerosol models depending on the M6 and M7 NIR bands. If the NIR bands are noisy, the erroneous aerosol correction is applied to the RSR in the visible bands. Chlorophyll retrieval algorithm results using the tainted RSR become less accurate.

The following procedure was used for our sensitivity study. TOA radiances were simulated for viewing geometries characteristic of the NPOESS 1:30 PM orbit on March 21, and for chlorophyll concentrations of 0.1, 1, and 5 mg m⁻³. The Morel (1988) reflectance model for Case 1 waters was used to simulate water-leaving radiance, and the 6S radiative transfer package was used to perform forward transfer to the TOA. Sensor noise was added to the simulated TOA radiances for each input chlorophyll concentration and for each of the VIIRS sensor performance models. One hundred random samples of the Gaussian noise distribution were obtained for each band and for each viewing geometry in a grid of 7 sensor zenith angles by 16 latitudes, covering the viewing swath. This provided 100 different maps of noise-added simulated radiance in each band. The Gordon-Wang atmospheric correction algorithm and the Carder et al. (1997) chlorophyll algorithm were applied to retrieve 100 different chlorophyll maps, and chlorophyll precision at each position was calculated as the standard deviation of the 100 chlorophyll values divided by the mean chlorophyll value. Thus, for each input value of chlorophyll concentration and each sensor performance model, maps of chlorophyll precision and mean retrieved chlorophyll concentration were obtained. Separate maps were also obtained of chlorophyll precision due to sensor noise in the visible bands and chlorophyll precision due to sensor noise in the NIR bands.

The full results of the sensitivity study are reported in reference [V-1] (see Section 1.3). Figure 11 shows that the precision specification on chlorophyll is not met for chlorophyll greater than 1

mg/m³. The result of interest here is that, for a given sensor performance model, noise in the near-infrared bands has a much smaller effect on chlorophyll precision than noise in the visible bands. This is shown in Figures 10 and 11. The reason is that, for a given measurement of TOA radiances, errors in the near-infrared bands lead to errors of the same sign in retrieved water-leaving radiance in the visible bands. (The atmospheric correction algorithm fits a model aerosol spectrum to the near-infrared bands, and the near-infrared errors cause the model fit to be either systematically high or systematically low in the visible bands.) The chlorophyll retrieval algorithm makes use of ratios of water-leaving radiance in different visible bands rather than absolute values of the radiance, and these ratios are less affected by sensor noise in the near-infrared bands than the absolute values of radiance are.

One of the NIR bands was located at 765 nm with a bandwidth of 40 nm. The final position of the NIR band is now at 746 nm with a bandwidth of 15 nm. The effects of sensor noise on chlorophyll precision had also been investigated for the case where a 10 nm wide band centered at 748 nm is used in place of the 40 nm wide band centered at 765 nm. This is intended to avoid the O₂ absorption feature at 762 nm. The narrower bandwidth results in greater sensor noise for a given VIIRS sensor performance model, but chlorophyll precision due to sensor noise gets only slightly worse. This is because sensor noise in the near-infrared bands still has a smaller effect on chlorophyll precision than sensor noise in the visible bands. Figure 12 shows a comparison of precision due to sensor noise for the different pairs of near-infrared bands, for the case of input chlorophyll concentration equal to 1.0 mg m⁻³.

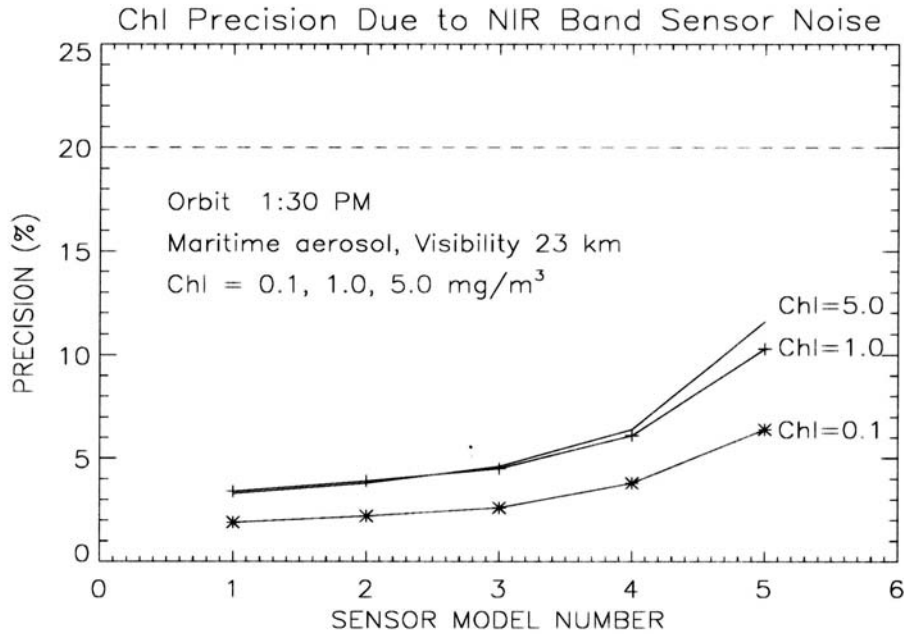


Figure 10. Mean chlorophyll precision due to sensor noise in the VIIRS near-IR bands as a function of VIIRS sensor performance model number. The precision values are averages for a 2400 km wide swath and solar zenith angle less than 70 degrees. The dashed line indicates the threshold requirement of 20 percent. The numbers on the x- axis represent models with worsening signal to noise ratio as the sensor model number increases. The Raytheon VIIRS final sensor noise level is between that given by sensor models 2 and 3.

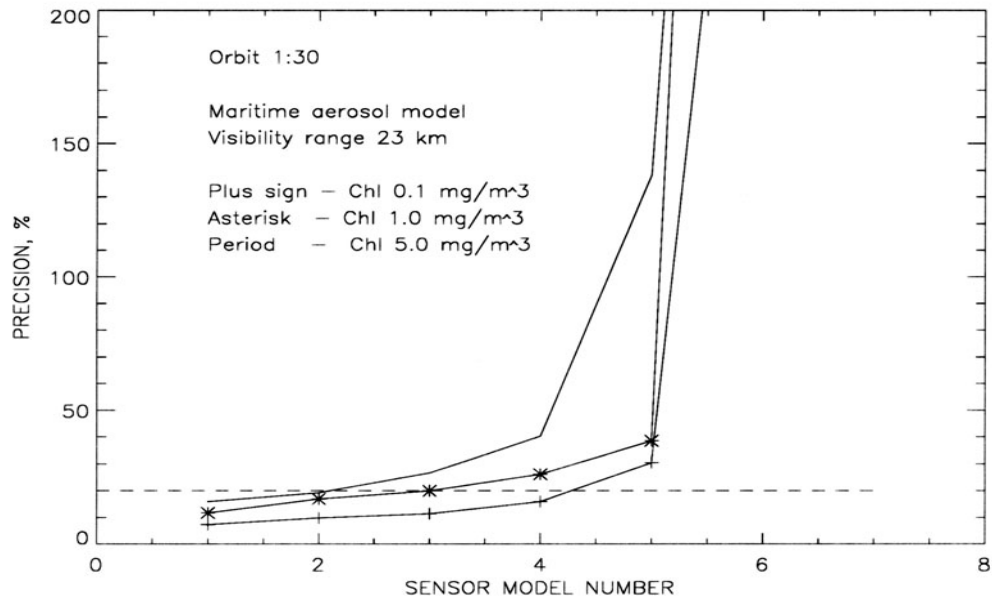


Figure 11. Mean chlorophyll precision due to sensor noise in the VIIRS visible bands as a function of VIIRS sensor performance model number. The precision values are averages for a 2400 km wide swath and solar zenith angle less than 70 degrees. The dashed line indicates the threshold requirement of 20 percent. The numbers on the x-axis represent models with worsening signal to noise ratio as the sensor model number increases. The Raytheon VIIRS final sensor is between that given by sensor models 2 and 3.

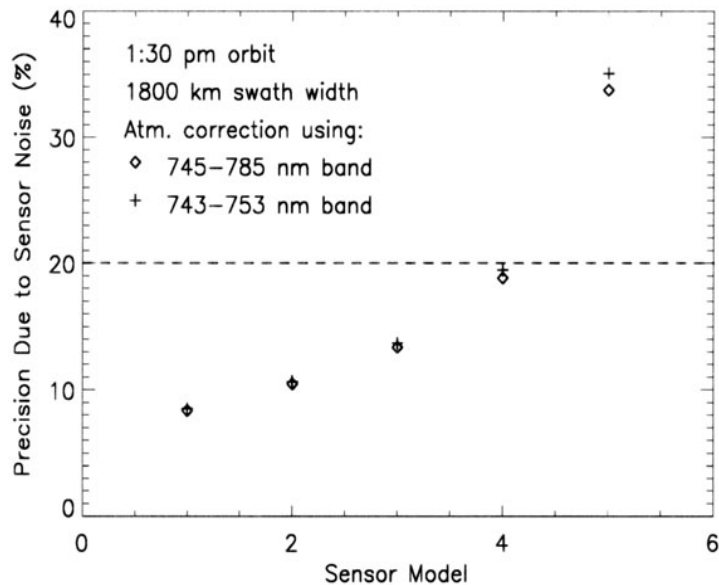


Figure 12. Chlorophyll precision due to sensor noise, averaged over the viewing swath of the 1:30 PM orbit, as a function of VIIRS sensor performance model.

3.4.3 Stray light effect

Stray light contamination of the TOA radiance for cloud-free pixels that are close to cloud, deserts, or vegetated areas may affect ocean color retrievals (chlorophyll and suspended particulate matter concentrations). Semi-infinite non-ocean areas adjacent to the ocean are considered. The semi-infinite case is believed to be the worst. A 20 km by 20 km cloud is also considered. A source of the stray light is assumed to be the instrumental scattered light. TOA radiances over the ocean were simulated in the VIIRS bands. Stray light errors simulated for different sensor optics models were added to the TOA radiances. Gaussian radiometric noise was also added to the simulated TOA radiances. To isolate chlorophyll errors due to the stray light contamination, a perfect atmospheric correction (simply the subtraction of the atmospheric path radiance from the TOA radiance) was applied to the TOA radiance. The Gordon-Wang atmospheric correction algorithm was also applied to the TOA radiance (Gordon and Wang, 1994). Chlorophyll was retrieved from the water-leaving radiance by using both the Carder bio-optical algorithm (Carder et al., 1997) and the standard SeaWiFS algorithm, OC2v (O'Reilly et al., 1998). Accuracy and precision were calculated as a function of a distance from the cloud edge.

Top of atmosphere radiances over the ocean were simulated at 413, 443, 488, 555, 770, and 865 nm (these are the VIIRS bands determined by Raytheon ITSS at the time of the ACO algorithm development) by using the 6S algorithm. This code uses the Morel reflectance model for Case 1 waters (Morel, 1988) to simulate water-leaving radiance for a given chlorophyll concentration and performs a forward transfer to the top of the atmosphere. The simulations were done for chlorophyll concentrations of 0.1, 1.0, and 5.0 mg/m³ and the following standard atmospheric parameters: water vapor content of 0.85 g/cm², ozone content of 0.395 cm-atm, maritime aerosol type, visibility of 23 km, and wind speed of 5 m/s. Geometric conditions correspond to the solar zenith angle of 40°, and viewing zenith angles of 0° and 45°, i.e. at the nadir and at the edge of a 1700 km swath. The pixel size was 1.3 km by 1.3 km.

The Morel (1988) reflectance model was chosen after comparing the predictions of three reflectance models with ship-based measurements from the SeaBAM dataset, which is described in the Ocean Color/Chlorophyll Flowdown Results document (Vasilkov and Odegard, 1998). The comparison showed that the Morel (1988) model provides the most realistic prediction of water-leaving radiance at low chlorophyll concentrations.

Stray light error was added to the simulated TOA radiance for each pixel by using the results of calculations done by G. Godden and M. Wang (personal communication, 1999) for different optics models with two band positions (left side of FPA, and right side of FPA). The fore-optics and aft-optics Point Spread Function (PSF) are modeled by Raytheon ITSS using a parameterization equation characterizing a specific sensor optics model. Semi-infinite cloud formation (a long straight cloud edge) with a well-defined cloud edge was assumed. The calculations were done for the ratio of radiances over the cloud and the ocean, i.e.,

$$\frac{L_{cloud}}{L_{ocean}} = 20 \quad (7)$$

Cloud shadow effect was not considered. A horizontal cell size was assumed to be equal to 1.3 km. The stray light model for the 20 km by 20 km cloud was quite similar. The error was

calculated along a line crossing the cloud center in a scan direction that was perpendicular to the cloud edge.

The stray light error was linearly scaled to the appropriate L_{cloud}/L_{ocean} values for the VIIRS visible and NIR bands. Cloud reflectance was assumed to be equal to 60%. The stray light error was introduced into the TOA radiance according to the following:

$$L(\lambda_i) = L_0(\lambda_i) \left[1 + \varepsilon_i \frac{R_{cloud}(\lambda_i)}{20R_{ocean}(\lambda_i)} \right] \quad (8)$$

where ε_i is the error in an i -th band calculated by the assumption given in Equation (7) and R is the TOA reflectance.

Sensor noise was added to the simulated TOA radiances for the baseline VIIRS sensor model 3 described by Hucks (1998). Noise equivalent delta radiance (NE Δ L) was calculated for a bandwidth of 20 nm at wavelengths 413, 443, 488, and 555 nm, which are used by the Carder algorithm. A random sample of the Gaussian noise distribution was obtained for each pixel. This provided about 300 different samples of noisy TOA and water-leaving radiances.

The retrieval of the chlorophyll concentration from the TOA radiances is performed in two steps: the atmospheric correction is performed to obtain remote sensing reflectance, and then a bio-optical algorithm is used to retrieve the chlorophyll concentration from the remote sensing reflectance. Two cases of the atmospheric correction were considered. To isolate chlorophyll errors due to the stray light contamination, a perfect atmospheric correction was first applied to the TOA radiance. The perfect atmospheric correction means that the atmospheric path radiance was simply subtracted from the simulated noise-added radiances. The Gordon-Wang atmospheric correction was also applied to the TOA radiance.

Chlorophyll precision was calculated as the standard deviation of the retrieved values divided by the mean chlorophyll value. Chlorophyll accuracy was calculated through the following relationship: $(mean - error_free)/error_free$, where *mean* is the mean retrieved chlorophyll and *error_free* is the retrieved chlorophyll value for the case where stray light error and sensor noise are not added to the simulated data. This definition of the chlorophyll accuracy based on the *error_free* value was used to avoid error due to the atmospheric correction itself and inconsistency between forward modeling of the TOA radiance and the Gordon-Wang atmospheric correction algorithm. The chlorophyll precision characterizes the effects of radiometric noise, and the chlorophyll accuracy characterizes the effects of stray light contamination.

A comparison of chlorophyll accuracy for the best (Raytheon ITSS developed VIIRS sensor model #4) and worst (Raytheon ITSS developed VIIRS sensor model #2) optics models is shown in Figure 13 for the case of a semi-infinite cloud with 60% reflectance. The solar zenith angle is 40°, the observation is at nadir, and the true chlorophyll concentration is 0.1 mg/m³. The chlorophyll accuracy is determined relative to the retrieved no-error chlorophyll value. No atmospheric correction removing stray light effects was applied. As it can be seen from Figure 13, the chlorophyll accuracy of 10% allocated for the stray light error source cannot be met within a 4 km area (or 3 pixels) adjacent to the cloud edge for the best model, Raytheon ITSS VIIRS sensor model 2. For the worst model, Raytheon ITSS VIIRS sensor model 4, about 12

pixels (16 km) adjacent to the cloud edge should be abandoned because the chlorophyll accuracy exceeds 10%.

It is interesting to note that the chlorophyll accuracy depends on the true chlorophyll concentration. Stray light effects are strongest for blue seawater, i.e. for low chlorophyll concentration. For no atmospheric correction removing stray light effects, stray light is simply added to the water-leaving radiance. If we approximate the spectral ratio of the cloud TOA reflectance to the ocean TOA reflectance to a power law function: $R_{cloud}/R_{ocean} \sim (\lambda/\lambda_0)^n$, the remote-sensing reflectance of seawater will be $R_{rs}(\lambda) + r_0 (\lambda/\lambda_0)^{n-1}$. Most bio-optical algorithms make use of band ratios, i.e. $R_{rs}(\lambda_i)/R_{rs}(\lambda_k)$. The simplest algorithm, OC2, uses a single ratio $R_{rs}(490)/R_{rs}(555)$. The more sophisticated Carder algorithm uses three band ratios as well as the absolute value of remote sensing reflectance at 555 nm. It is obvious that stray light contamination will not affect chlorophyll retrievals of band-ratio algorithms if the spectral behavior of the remote sensing reflectance, $R_{rs}(\lambda)$, obeys the power law function $(\lambda/\lambda_0)^{n-1}$. The spectral behavior of the remote sensing reflectance, $R_{rs}(\lambda)$, is determined by the chlorophyll concentration. Thus, one can expect that for some range of chlorophyll concentrations the stray light effects would be minimal.

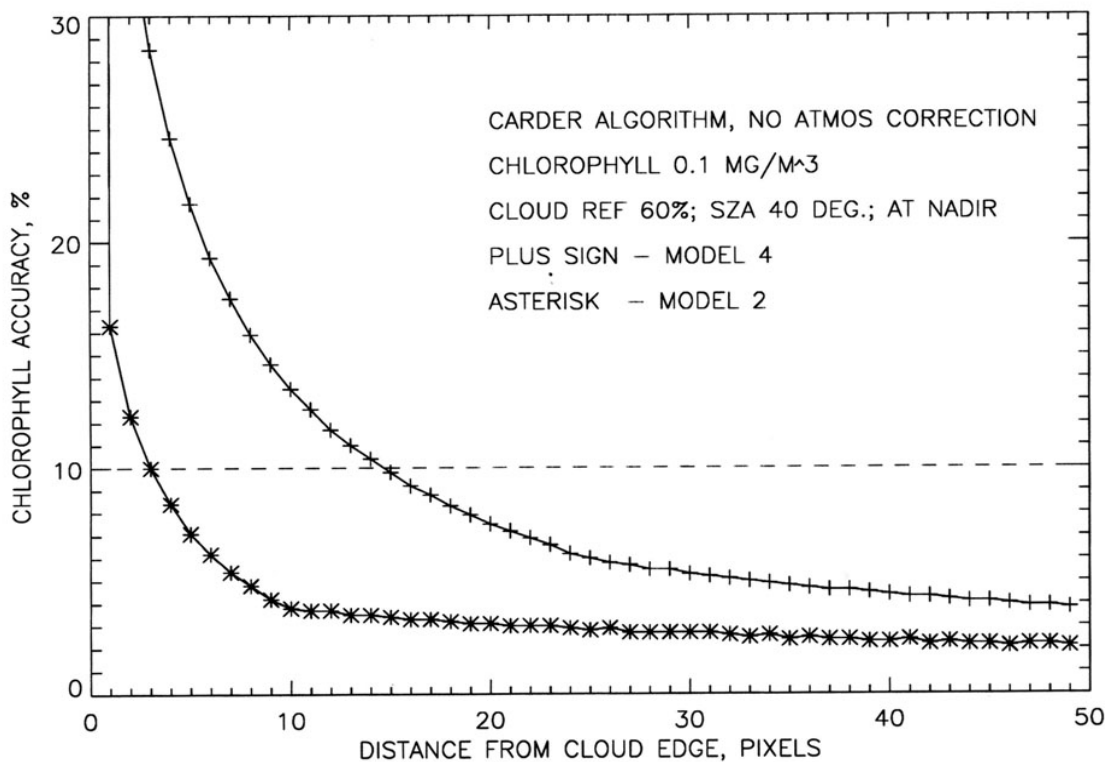


Figure 13. Chlorophyll accuracy as a function of a distance from the edge of a semi-infinite cloud. A dashed line represents the accuracy of 10% allocated for the stray light error source.

A comparison of the chlorophyll accuracy for the OC2 and Carder algorithms showed that the performance of the Carder algorithm is somewhat better than the OC2 algorithm performance.

Calculations done for the viewing zenith angle of 40° showed that the chlorophyll accuracy due to stray light contamination is slightly worse than for nadir observation at the same distance from the cloud edge.

Using the Gordon-Wang atmospheric correction algorithm dramatically changes the results described above. The atmospheric correction effectively removes the stray light contamination from the TOA radiances. A comparison of the chlorophyll accuracy for the cases of no atmospheric correction removing the stray light contamination and the Gordon-Wang atmospheric correction is shown in Figure 14. It can be seen that the stray light effects on the chlorophyll retrievals have practically been removed except for one pixel adjacent to the cloud edge. The chlorophyll accuracy due to stray light contamination is better than 3% except the pixel adjacent to the cloud edge. It has been mentioned that the spectral stray light contamination can be approximated by the power law: $(\lambda/\lambda_0)^{n-1}$. The atmospheric correction effectively interprets this contamination as a virtual aerosol contribution to the TOA radiance.

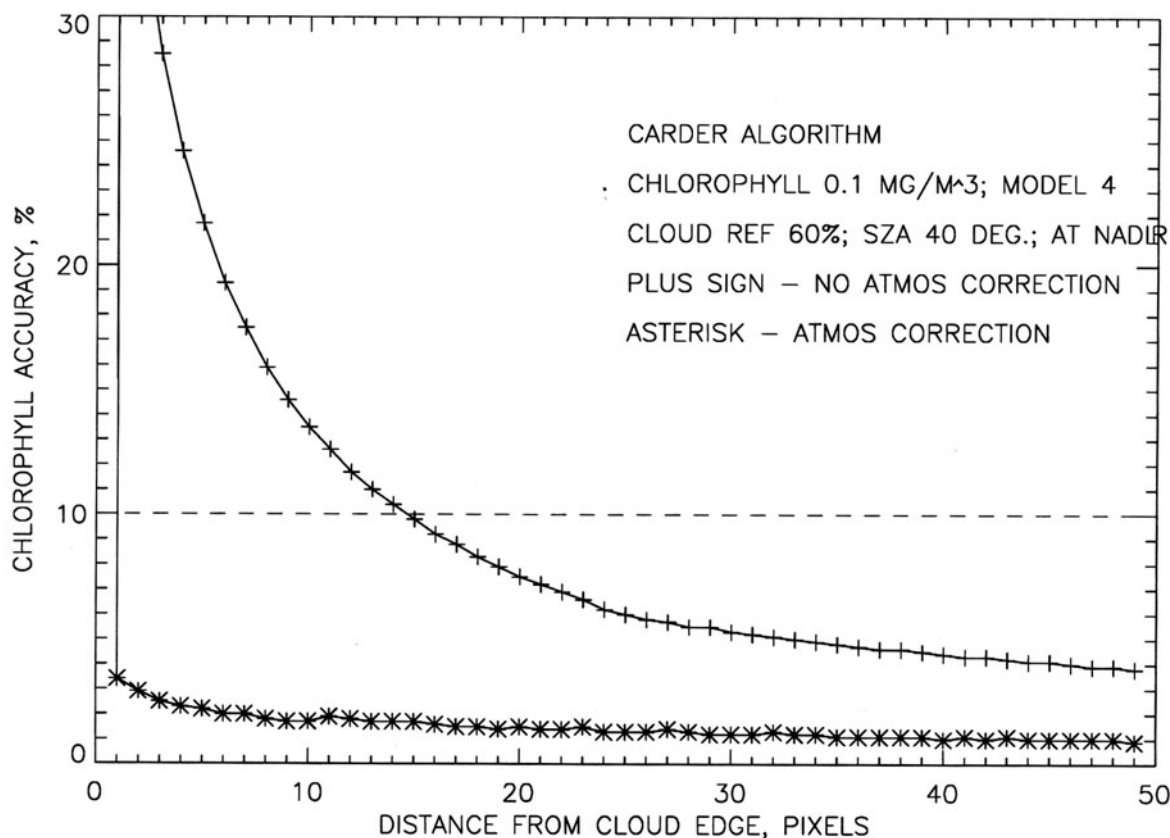


Figure 14. Comparison of the chlorophyll accuracy obtained with no atmospheric correction and the Gordon-Wang atmospheric correction algorithm. A dashed line represents the accuracy of 10% allocated for the stray light error source.

Semi-infinite desert and green vegetation areas adjacent to the ocean were also considered. It should be noted that for the case of green vegetation the true atmospheric correction was absolutely necessary to estimate stray light effects on chlorophyll retrievals. This is explained by the fact that the vegetation reflectance is low in the visible bands and very high in the NIR bands. A comparison of the chlorophyll accuracy for cases of white cloud, sand, and green vegetation is shown in Figure 15. The stray light contamination caused by green vegetation affects the chlorophyll accuracy the most. The chlorophyll accuracy is worse than the 10% allocated for the stray light error source within at least three pixels (about 4 km) adjacent to the border between the ocean and terrain considered.

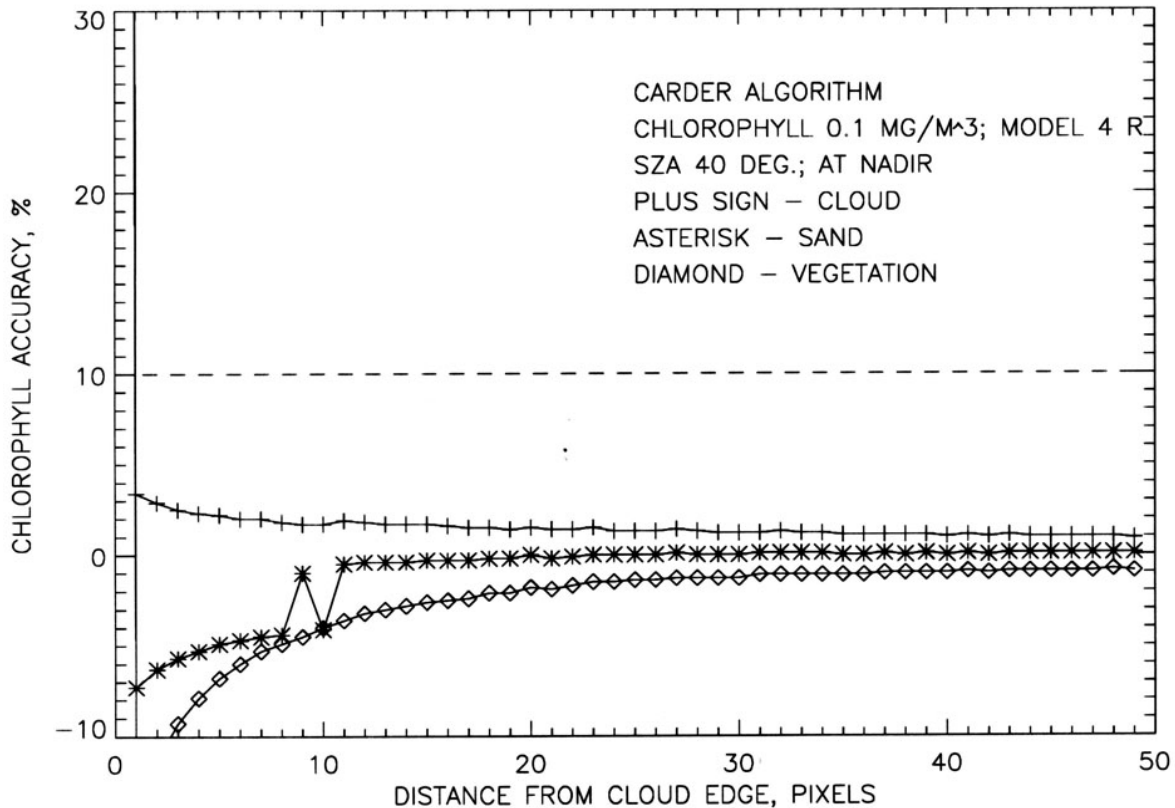


Figure 15. Comparison of the chlorophyll accuracy calculated for a semi-infinite cloud, desert, and vegetation. The Gordon-Wang atmospheric correction algorithm was applied to the TOA radiances.

The chlorophyll accuracy was also compared for the limited and semi-infinite clouds for the case of the Gordon-Wang atmospheric correction algorithm applied to the TOA radiances. The comparison is shown in Figure 16. The atmospheric correction effectively removes stray light effects for both the semi-infinite cloud and the limited cloud except for a couple of pixels adjacent to the cloud edge. The chlorophyll accuracy is slightly worse in the case of the semi-infinite cloud.

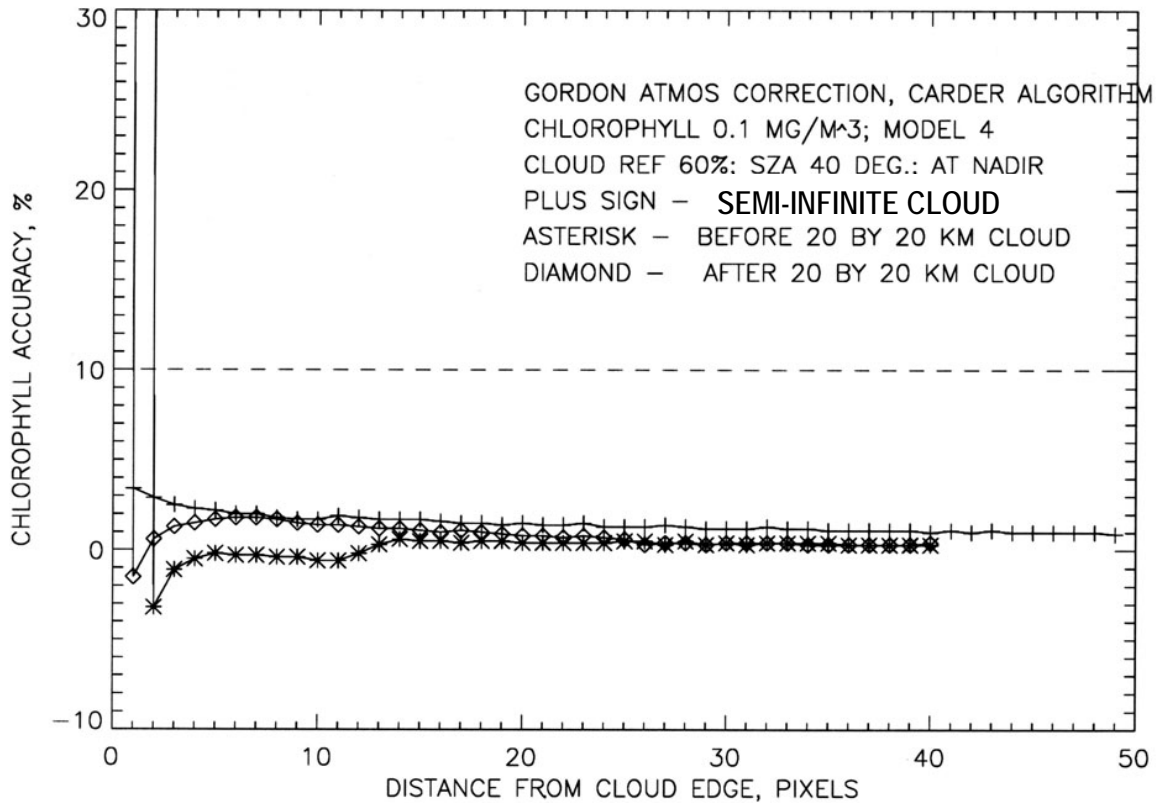


Figure 16. Comparison of the chlorophyll accuracy calculated for the semi-infinite and limited clouds using the Gordon-Wang atmospheric correction.

The atmospheric correction algorithm is able to effectively remove the stray light effects in which the spectral behavior is similar to the spectral contribution of aerosol to the TOA radiance. In the case of the effective removal of stray light contamination only one pixel adjacent to the cloud edge should be abandoned because it does not meet the chlorophyll accuracy of 10% allocated for the stray light error source. The stray light contamination due to a semi-infinite vegetated area adjacent to the ocean has a greater affect on the chlorophyll retrievals than a semi-infinite cloud does. The chlorophyll accuracy is worse than 10% within three pixels (about 4 km) adjacent to the border between the ocean and vegetated area.

3.4.4 Residual instrumental polarization

The quality of bio-optical products from satellite ocean color sensors is strongly dependent on the accuracy of sensor measurements of the top-of-the-atmosphere (TOA) radiance. Radiation measured at the top of the atmosphere is generally polarized. Because all color sensors have some polarization sensitivity, the radiance measured by the sensor will be biased. This error in the TOA radiance due to the instrumental polarization sensitivity can affect the accuracy of the final bio-optical product of the ocean color sensors. It is of practical interest to estimate how well atmospheric correction and bio-optical algorithms can tolerate significant instrumental polarization. The performance of bio-optical algorithms may vary for polarization-induced errors depending on the particular algorithm. The acceptable magnitude of the sensor polarization

sensitivity should be determined from the bio-optical product error allocated for polarization-induced error source.

Basically, there are two options for estimating the acceptable magnitude of the sensor polarization sensitivity. If the polarization state of the TOA radiation is not accounted for by an atmospheric correction algorithm, the requirement for the sensor polarization sensitivity should be the acceptable maximum. However, if the atmospheric correction algorithm allows correction for the polarization-induced error, requirements for the sensor polarization sensitivity should be formulated. This characterization should include both the amplitude and phase angle of the sensor polarization sensitivity.

The sensor-measured Stokes vector \mathbf{I}_m can be represented by:

$$\mathbf{I}_m = \mathbf{M} \mathbf{R}(\alpha) \mathbf{I}_t \quad (9)$$

where $\mathbf{I}_t = \{I, Q, U, V\}$ is the TOA Stokes Vector, $\mathbf{R}(\alpha)$ is the rotation matrix transferring \mathbf{I}_t from the calculation-based reference plane, which contains the propagation direction of the light and the vertical axis, to the instrument-based reference plane, α is the angle between the two reference planes, and \mathbf{M} is the instrument Mueller matrix, describing the sensor response to the input Stokes vector. The first element m_{11} of \mathbf{M} can be taken as 1 by the calibration. The measured intensity I_m then is:

$$I_m = I_t + m_{12}(Q_t \cos 2\alpha + U_t \sin 2\alpha) + m_{13}(-Q_t \sin 2\alpha + U_t \cos 2\alpha) \quad (10)$$

where we neglect the component V_t . By introducing the degree of the polarization, P , of the TOA light

$$\frac{Q_t}{I_t} = P \cos 2\varphi, \quad \frac{U_t}{I_t} = P \sin 2\varphi,$$

$$\varphi = \frac{1}{2} \arctan\left(\frac{U_t}{Q_t}\right)$$

and using the instrument polarization sensitivity, P_{in} , and polarization phase angle, χ_{in} ,

$$m_{12} = P_{in} \cos 2\chi_{in}, \quad m_{13} = P_{in} \sin 2\chi_{in}$$

we can rewrite (10) in the following form:

$$I_m = I_t [1 + P_{in} P \cos 2(\alpha - \varphi - \chi_{in})] \quad (11)$$

The relative error of the measurement of intensity can be represented as:

$$\frac{\Delta I_t}{I_t} \equiv \frac{I_m - I_t}{I_t} = P P_{in} \cos 2(\alpha - \varphi - \chi_{in}) \leq P P_{in} \quad (12)$$

The instrumental polarization sensitivity is a measure of the sensor response to completely linear polarized light. It is defined as:

$$P_{in} = \frac{I_{max} - I_{min}}{I_{max} + I_{min}} \quad (13)$$

where I_{max} and I_{min} are the maximum and minimum of the measured radiance for linearly polarized source radiance for which the plane of polarization contains the line of sight and has any orientation about the line of sight. In practice, the instrumental polarization sensitivity is known with some error ΔP_{in} and the polarization phase angle is known with some error $\Delta\chi_{in}$.

The problem of the effects of the instrumental polarization sensitivity on bio-optical retrievals can be formulated as follows. Given the uncertainty in the bio-optical product allocated for polarization-induced error, one should derive the requirements for the instrumental polarization sensitivity and phase angle assuming at least the two following cases: The first case is an atmospheric correction algorithm not accounting for the polarization state of TOA radiation. The requirement for this case should set up an acceptable maximum for the sensor polarization sensitivity, P_{in} . The uncertainties in the sensor polarization sensitivity and phase angle do not play a role. The second case is an atmospheric correction algorithm accounting for the polarization state of TOA radiation. The acceptable maximum for the sensor polarization sensitivity should be established in this case as well but this should be accompanied by requirements to sensor polarization characterization including the uncertainties in the sensor polarization sensitivity, ΔP_{in} , and phase angle, $\Delta\chi_{in}$. These requirements strongly depend on the manner of polarization correction introduced in the atmospheric correction algorithm. All of the above requirements should also be considered from the point of view of their technical feasibility because the polarization requirements may be contradictory to other sensor requirements. For example, using a polarization scrambler may not be feasible for a specific sensor because of its deterioration of sensor stray light characteristics.

The degree of linear polarization (P, a measure of the polarization of the atmosphere-Earth source system) for VIIRS is between 0 and 60% (25% is a typical value at 443 nm; see Figure 17). Linear polarization decreases with the increase of the aerosol optical thickness (Figure 18). For a given aerosol optical depth, the linear polarization depends slightly on aerosol type (Figure 19). The measurement error in radiance/reflectance results from the residual instrumental polarization depends on residual instrumental polarization sensitivity (P_{int}), polarization angle (c_{int}), and P of the radiation source.

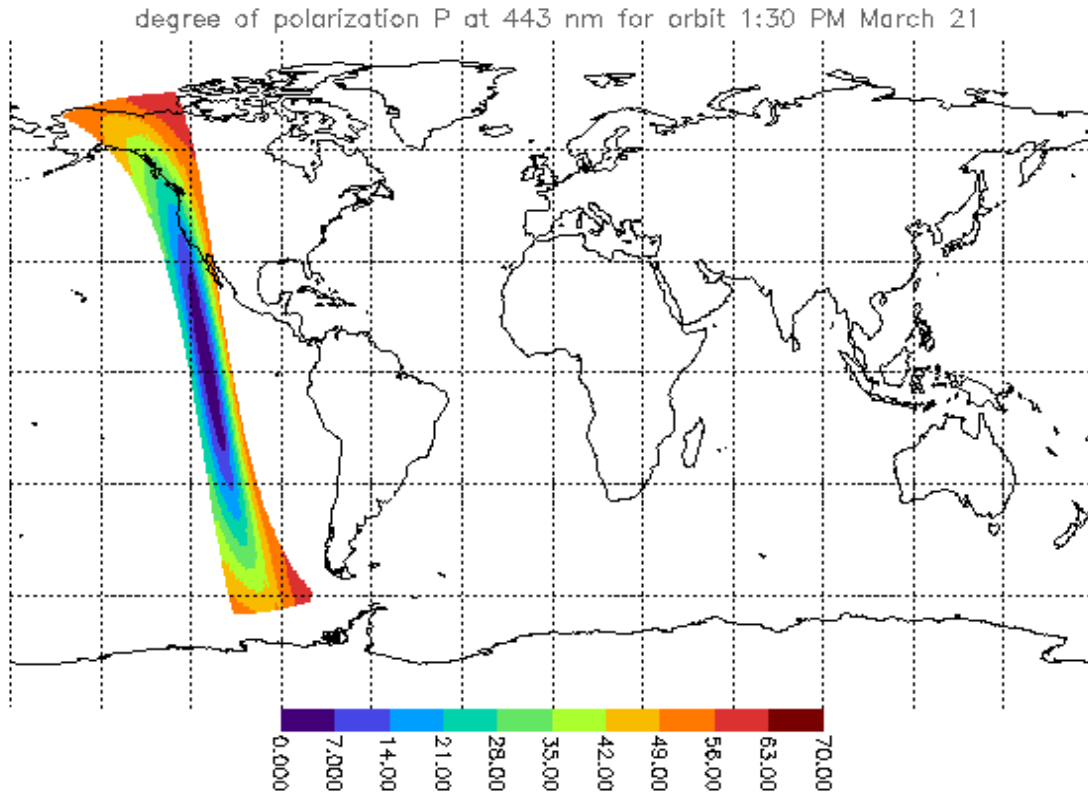


Figure 17. Degree of polarization at 443 nm.

For a stressing case (low sun and viewing angle of 47 degree) and a residual instrument polarization sensitivity of 2%, the relative error on radiance/reflectance at blue bands from Eq.(12) is approximately 1.5%. The 1.5% error in TOA radiance can result in a 15% error for the remote sensing reflectance. A correction is required for 3% residual instrumental polarization for the stressing case.

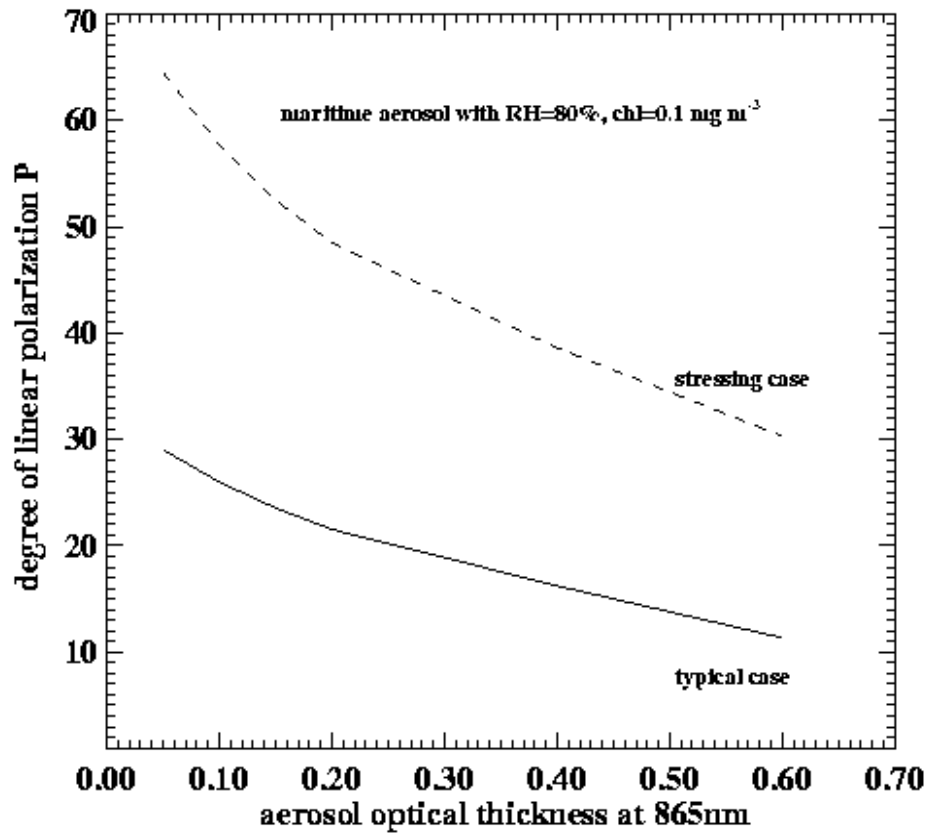


Figure 18. Variation of linear polarization with the optical depth of the aerosol.

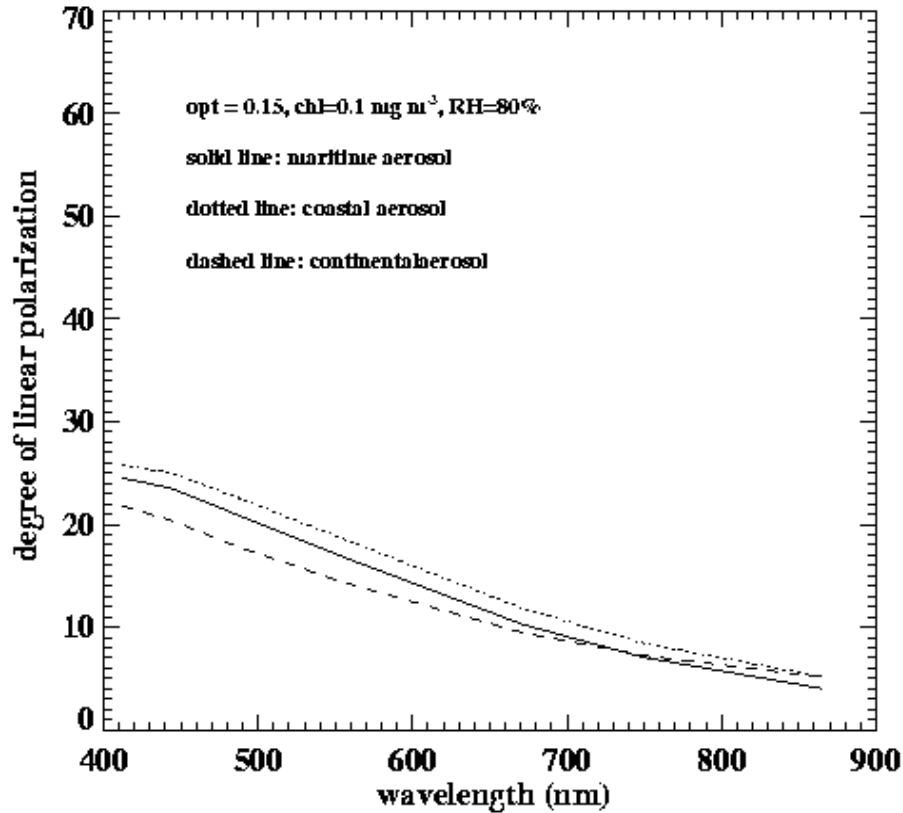


Figure 19. Dependency of linear polarization on aerosol type with sun zenith = 41 degree, viewing = 30 degree, Relative azimuth = 90 degree, chlorophyll = 0.1 mg/m³

Gordon et al. (1997b) have studied the effect of the residual instrumental polarization on the water-leaving radiance. They have developed a two-step algorithm to reduce the effect of the residual polarization error. The algorithm uses the Gordon-Wang algorithm and look-up tables based on fully polarized code. Using optical thickness and aerosol type from the first step to correct residual polarization, the atmospheric correction algorithm is performed again. The two-step algorithm reduces the error of the chlorophyll concentration retrieval dramatically (Figure 20). This two-step algorithm may be worth considering if the residual instrumental polarization for VIIRS is turned out to be important after the sensor characterization.

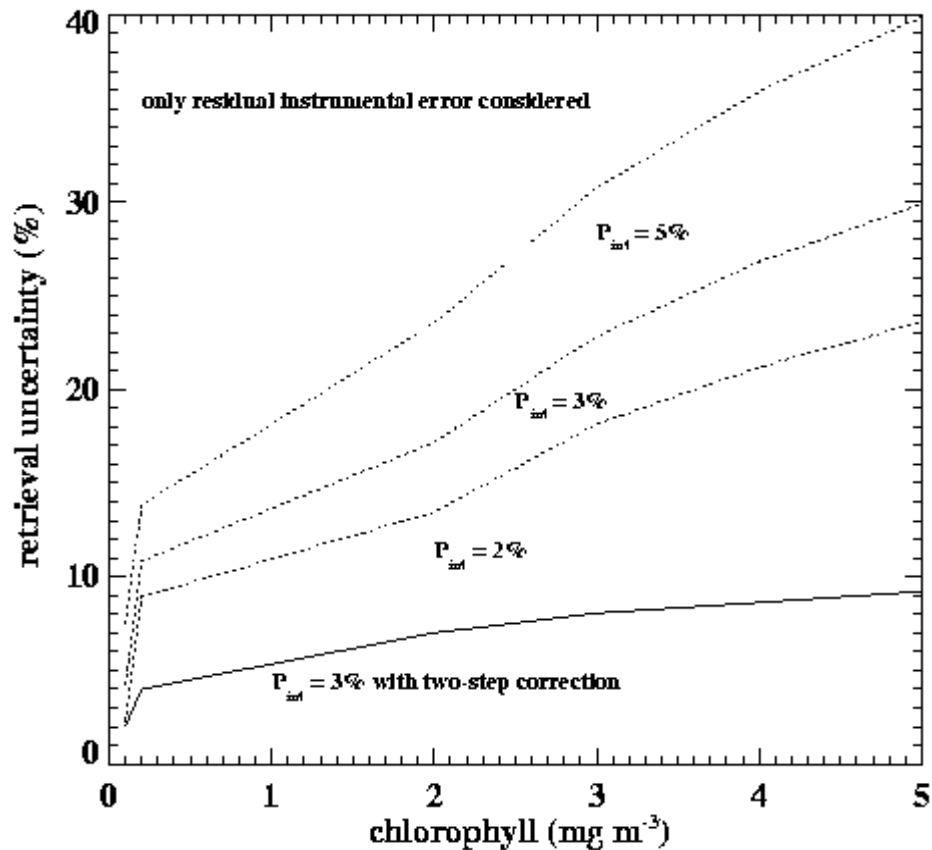


Figure 20. Retrieval uncertainty for various polarization sensitivities. The two-step algorithm yields the best results.

3.4.5 Absorbing aerosols

There are no chlorophyll retrievals in huge areas of the Atlantic Ocean from SeaWiFS. Those areas have been masked by SeaWiFS because the atmospheric correction algorithm resulted in negative water-leaving radiances. This atmospheric correction algorithm failure is caused by Saharan dust blown over the ocean by the westward winds. Maritime aerosol is non-absorptive because its single scattering albedo is about 1 at 555 nm. The single scattering albedo for desert dust aerosol is about 0.8 in the winter; therefore desert dust aerosol is absorbing aerosol. In addition, the epsilon value for non-absorbing and absorbing aerosols is quite different (see Figure 21). We have included desert, urban, and volcanic aerosols in the look-up table so that the algorithm can treat absorbing aerosols. However, the problem of absorbing aerosols is quite complex.

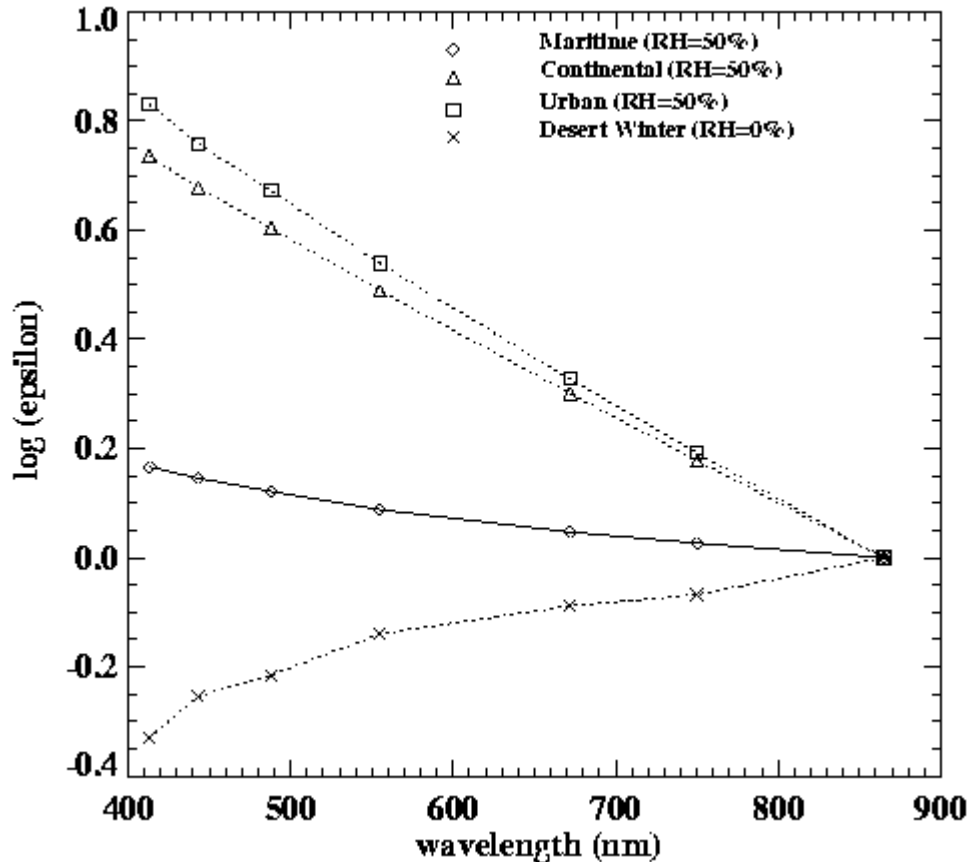


Figure 21. Variation of $\epsilon(\lambda, 865)$ for nadir viewing with a sun zenith angle of 41° for the maritime, continental and urban aerosol models for RH=50% and a desert aerosol (wintertime) with RH=0%.

3.5 PRACTICAL CONSIDERATIONS

3.5.1 Numerical Computation Considerations

Information on computation speed can be found in the VIIRS Computer Resource Requirements [Y-3257].

3.5.2 Correction to the Instrumental Polarization

The specification value for the instrumental polarization sensitivity is 3%. By the end of phase II, RAYTHEON has achieved a much better design than the specification value for the polarization sensitivity (see chart 189, VIIRS Sensor Technical Interchange Meeting, November 27-29, 2001). The instrumental residual polarization sensitivity for NIR bands is as low as about 0.5%. This value implies that a SeaWiFS/MODIS like standard atmospheric correction algorithm can be used along with a polarization correction for the blue, green, and yellow bands. The polarization correction algorithm has actually been implemented for all of the VIIRS ocean color bands.

3.5.3 Stray Light Warning Flag

Scatter light is defined as light contamination from the instrument itself, for example the instrument surface roughness. Stray light is defined as the effect of inhomogeneous scenes, such as a scene composed of cloud and clear ocean surface. In practice, the scatter light and stray light cannot be strictly separated. In this section, we discuss the stray light flag only.

As shown in Figure 14, the chlorophyll accuracy of 10% allocated for the stray light error source can be met, except within a pixel of a cloud edge. In these circumstances, atmospheric correction processing will still be carried out, but the cloud adjacency flag from the VIIRS Cloud Mask will be passed along as a warning that stray light contamination from clouds is possible. Stray light contamination for pixels adjacent to land is also possible, but atmospheric correction will also be carried out in these cases as well. Pixels adjacent to land are likely to be flagged as coastal, shallow water, or turbid.

In addition, VIIRS SDR produces the Bright Pixel I.D. to flag the scattered light contaminated pixels (detailed description is given in a NGAS Technical Memo, NP-EMD.2007.510.0011 Rev A). The ocean color implementation of the Bright Pixel flag is described in another NGAS Technical Memo, NP-EMD.2007.510.0051.

3.5.4 Programming and Procedural Considerations

The ACO algorithm is the first algorithm in the Ocean Color processing chain. It provides the RSR IP as input for OCC processing to produce the ocean color EDR in the second algorithm in the chain.

3.5.5 Quality Assessment and Diagnostics

Flags are given to indicate the quality of the retrieval. Flags indicate valid data, negative water leaving radiance, cloud contamination, turbid water, shallow water, and absorbing aerosol.

3.5.6 Exception Handling

Exceptions will occasionally prevent operation of the algorithm, such as missing VIIRS data or unavailable ancillary data. Errors in retrieved remote sensing reflectance can also cause exceptions in algorithms that use remote sensing reflectance as inputs. A set of flags is given to indicate situations when atmospheric correction should not be attempted, when the algorithm fails, or when the retrieved values are not realistic (e.g., negative values of remote sensing reflectance).

3.6 ALGORITHM VALIDATION

3.6.1 Error Budget

Performing the following steps generated the error budget:

- a) Utilizing a perfect sensor and perfect ancillary/auxiliary inputs.

- b) Introducing error in the ancillary/auxiliary inputs.
- c) Introducing the radiometric noise.
- d) Introducing the calibration stability error.
- e) Introducing residual instrumental polarization sensitivity.

The error due to stray light is estimated. The band-to-band registration error is small and negligible. The error due to “cloud masked where clear” does not affect the error budget. See the VIIRS Error Budget [Y-3249] document for further details of the error budget. According to this error budget document [Y-3249], the performance (i.e. using predicted radiometric noise) for fine resolution is better than the specification value.

3.6.2 Global maps of remote sensing reflectance and retrieval of chlorophyll

The chlorophyll concentration was used as input for our forward radiative transfer model. Maritime aerosol with relative humidity of 80% and a visibility of 23 km is used. Sun glint was not considered in the calculation because the overlap of the 9:30 AM and 1:30 PM orbits can eliminate most parts of the area contaminated by sun glint. It can be seen from Figure 22 that low remote sensing reflectance occurs in areas with high chlorophyll concentration. The retrieval algorithm for the chlorophyll concentration uses the remote sensing reflectance at 413, 445, 488, 555 nm. The chlorophyll retrieval uncertainties are given in Figure 23.

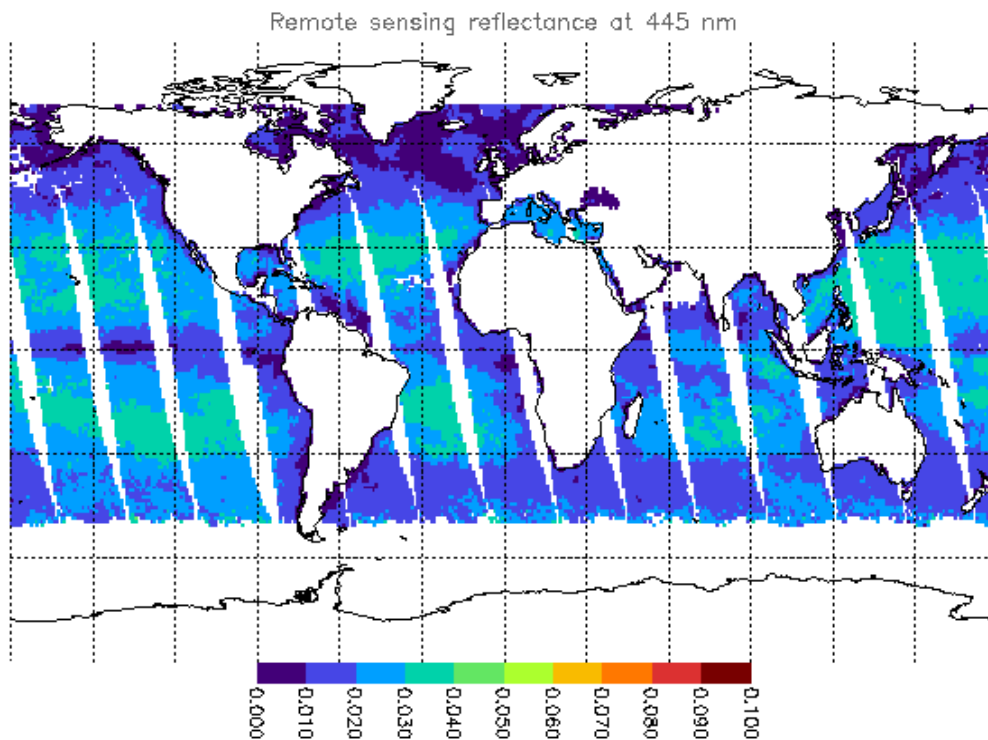


Figure 22. Retrieved remote sensing reflectance.

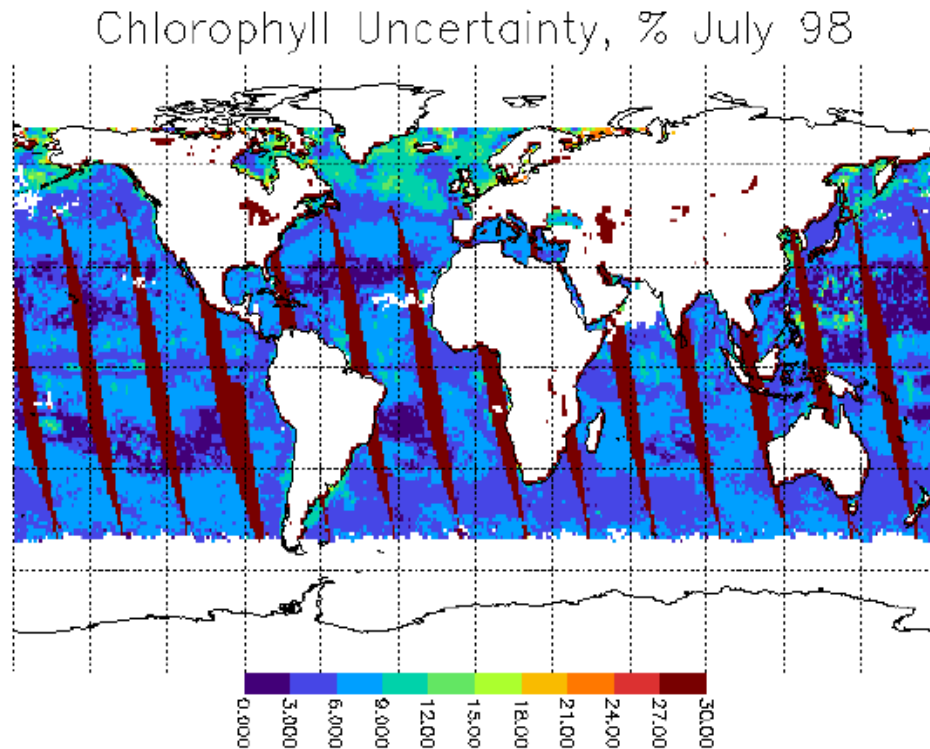


Figure 23. Uncertainty of the retrieval of the chlorophyll concentration.

3.6.3 Post-launch validation

Post-launch validation of retrieved remote sensing reflectance will make use of VIIRS solar and lunar measurements, and vicarious calibration using measurements made at the ocean surface from fixed moorings and ships. The validation approach for VIIRS incorporates methods developed for SeaWiFS and MODIS validation (McClain et al., 1992; Mueller and Austin, 1995; Clark et al., 1997). Measurements of an onboard calibration source and measurements of an onboard solar diffuser will be used to correct for any short-term variations in sensor stability in each wavelength band. Vicarious calibration will be performed after any such time-dependent corrections are applied to the VIIRS data.

Vicarious calibration will make use of measurements of remote sensing reflectance in the VIIRS 412, 445, 488, 555, and 672 nm bands from fixed buoys and ships at open ocean sites characterized by optically clear water and marine aerosols. These measurements will be made simultaneously with VIIRS retrievals of remote sensing reflectance for pixels containing the sites. Retrieved and *in situ* reflectance values will be compared to obtain a calibration gain correction factor for each wavelength band. Ratios of retrieved to *in situ* reflectance for each band will be examined for any trend with time or with atmospheric path length, to check for possible errors in the time-dependent calibration gain factors or possible deficiencies of the

atmospheric correction algorithm. Temporal trends will also be identified in retrieved values of remote sensing reflectance for open ocean, clear water (retrieved chl $a < 0.15 \text{ mg m}^{-3}$) pixels.

This vicarious calibration method cannot be applied to the VIIRS M6 and M7 (746 and 865 nm) bands because the atmospheric correction algorithm assumes water-leaving reflectance values are zero in these bands. The pre-launch calibration of the M7 band will be assumed to be correct, and a calibration gain correction factor for the M6 band will be determined assuming $\epsilon(746,865) = 1.0$, which is typical of marine aerosols. (The quantity $\epsilon(746,865)$ is the 746 nm to 865 nm band ratio of single scattering aerosol reflectance.) This correction factor is determined by comparing the ratio of measured VIIRS radiances in the M6 and M7 bands, averaged over many measurements of the calibration sites, with the ratio predicted by a radiative transfer calculation for $\epsilon(746,865) = 1.0$.

This method of vicarious calibration has been applied to SeaWiFS data using surface measurements from the marine optical buoy (MOBY) located off of Hawaii, and the calibration has been verified using ship-based measurements such as those from the Atlantic Meridional Transect Program (Robins et al., 1996). A similar vicarious calibration procedure is required for VIIRS data using surface measurements from MOBY and any other fixed open-ocean optical measurement moorings that may be operational in the NPOESS era. After application of vicarious calibration, retrieval of remote sensing reflectance will be validated for a wide range of geophysical conditions using surface measurements from NPOESS validation cruises that will take place shortly after the NPOESS launch, as well as from any cruises that may take place at roughly the same time for calibration and validation of other ocean color sensors.

Validation should be performed for conditions that are difficult for atmospheric correction, including the presence of urban aerosols, desert dust, stratospheric aerosols and/or thin cirrus clouds, turbid coastal waters, whitecaps, and broken cloud fields or islands (to examine the effect of stray light on atmospheric correction). Clark et al. (1997) have described plans for validation of MODIS atmospheric correction under these conditions. Surface measurements to be performed include measurement of water-leaving radiance in the direction of the sensor, chlorophyll concentration in the vicinity of the ship, spectral aerosol optical thickness and spectral sky radiance at angles close to and far from the solar zenith and azimuth angles, vertical aerosol distribution using lidar, and spectral whitecap radiance. Results of validation studies for SeaWiFS, MODIS, and other pre-NPOESS ocean color sensors will be taken into account in development of a detailed validation plan for VIIRS.

3.7 ALGORITHM DEVELOPMENT ACTIVITIES (P³I)

For turbid water, we may apply the algorithm developed by Hu et al. (1999, private communication). This algorithm applies the aerosol properties over less turbid water to the turbid water. For shallow water, we may use the same concept. These algorithms need to be extended for our operational scheme. For the absorbing aerosols, our algorithms can treat desert and volcanic aerosols, but work on these cases is not complete and needs to continue.

4.0 ASSUMPTIONS AND LIMITATIONS

4.1 ASSUMPTIONS

The Gordon-Wang algorithm makes use of the following assumptions:

- (1) The aerosol models used are representative of aerosols present over global ocean.
- (2) Water-leaving reflectance is zero in the two near-infrared wavelength bands (VIIRS M6 and M7).
- (3) The formulation of whitecap reflectance as a function of wind speed and electromagnetic wavelength is valid.
- (4) The two-layer plane-parallel model atmosphere adopted for radiative transfer calculations is valid.
- (5) The BRDF, cloud shadow, and out-of-band response are negligible.

4.2 LIMITATIONS

The assumptions listed above are not always valid:

- (1) The algorithm performs poorly in cases where strongly absorbing aerosols are present.
- (2) Water-leaving reflectance in the NIR bands is not negligible in turbid coastal waters or in coccolithophore blooms.
- (3) Further studies of the dependence of whitecap reflectance and the magnitude of its contribution at the TOA on wind speed and wavelength should be made.

5.0 ACKNOWLEDGEMENTS

The authors of Version 5 of this ATBD would like to acknowledge Nils Odegard and Alexander Vasilkov, authors of the Version 4 ATBD, on which this version is based. We would also like to acknowledge a former Science Team Member, Menghua Wang of the University of Maryland Joint Center for Earth Systems Technology, who also made contributions to the development of previous versions of this ATBD.

6.0 REFERENCES

- Carder, K., S. Hawes, and R.F. Chen (1997). Case 2 Chlorophyll_a Algorithm and Case 2 Absorption Coefficient Algorithm. MODIS ATBD 19.
- Clark, D.K., H.R. Gordon, K.J. Voss, Y. Ge, W. Broenkow, and C. Trees (1997). Validation of atmospheric correction over ocean. *J. Geophys. Res.*, 102, 17209.
- Cox, C., and W. Munk (1954). Measurements of the roughness of the sea surface from photographs of the sun's glitter. *J. Opt. Soc. Amer.*, 44, 838.
- Frouin, R., M. Schwindling, and P.-Y. Deschamps (1996). Spectral reflectance of sea foam in the visible and near-infrared: In situ measurements and remote sensing implications *J. Geophys. Res.*, 101, 14361.
- Gordon, H.R., and K.J. Voss (1999). Normalized Water-leaving Radiance Algorithm Theoretical Basis Document. MODIS ATBD 17 (April 30, 1999).
- Gordon, H.R. (1997a). Atmospheric correction of ocean color imagery in the Earth Observing System era. *J. Geophys. Res.*, 102, 17081.
- Gordon, H. R., Tao Du, and Tianming Zhang (1997b), Atmospheric correction of ocean color sensors: analysis of the effects of residual instrument polarization sensitivity. *Appl. Opt.*, Vol. 36, pp. 6938-6948.
- Gordon, H.R., J.W. Brown, and R.H. Evans (1988). Exact Rayleigh scattering calculations for use with the Nimbus-7 coastal zone color scanner. *Applied Optics*, 27, 862.
- Gordon, H.R., D.K. Clark, J.W. Brown, O.B. Brown, R.H. Evans, and W.W. Broenkow (1983). Phytoplankton pigment concentrations in the Middle Atlantic Bight: comparison between ship determinations and Coastal Zone Color Scanner estimates. *Applied Optics*, 22, 20.
- Gordon, H.R., and A.Y. Morel (1983). *Remote Assessment of Ocean Color for Interpretation of Satellite Visible Imagery: A Review*. New York: Springer-Verlag, p. 114.
- Gordon, H.R., and M. Wang (1992). Surface roughness considerations for atmospheric correction of ocean color sensors. 1. The Rayleigh scattering component. *Applied Optics*, 31, 4247.
- Gordon, H.R., and M. Wang (1994a). Retrieval of water-leaving radiance and aerosol optical thickness over the oceans with SeaWiFS: a preliminary algorithm. *Applied Optics*, 33, 443.
- Gordon, H.R., and M. Wang (1994b). Influence of oceanic whitecaps on atmospheric correction of SeaWiFS. *Applied Optics*, 33, 7754.
- Herring, David. (1997). Marine optical buoy (MOBY) Evolves, while marine optical characterization experiment (MOCE) continues in support of SeaWiFS, MODIS, and OCTS, *The Earth Observer*, Vol. 9, No. 5, 15-20.
- Hu, C., K. Carder, F. Muller-Karger (1999). Atmospheric correction of SeaWiFS imagery over turbid coastal water (private communication).

- Hucks, J. (1998). RSTX Internal Memorandum Y1629.
- Koepke, P. (1984). Effective Reflectance of Oceanic Whitecaps. *Applied Optics*, 23, 1816.
- Ladner, S.D., R.W. Gould, R.A. Arnone, and P.M. Martinolich (1998). Comparison of ship and SeaWiFS-derived reflectances and inherent optical properties. In *Proceedings of the Fifth International Conference on Remote Sensing for Marine and Coastal Environments*, Vol. I, p. 449.
- McClain, C.R., W.E. Esaias, W. Barnes, B. Guenther, D. Endres, S.B. Hooker, B.G. Mitchell, and R. Barnes (1992). SeaWiFS calibration and validation plan. *SeaWiFS Technical Report Series*, Vol. 3.
- McClain, C.R., Eueng-Nan Yeh, (1994). Sun Glint Flag Sensitivity Study. *SeaWiFS Technical Report Series*, Vol. 13, NASA Technical Memorandum 104566.
- Morel, A. (1988). Optical modelling of the upper ocean in relation to its biogenous matter content (Case 1 waters). *J. Geophys. Res.*, 93, 10749.
- Mueller, J.L., and R.W. Austin (1995). Ocean optics protocols for SeaWiFS validation, Revision 1. NASA Tech. Memo. 104566, Vol. 25, S. B. Hooker and E. R. Firestone, Eds., NASA Goddard Space Flight Center.
- Odegard N. and Vasilkov A.P. 1998, Raytheon ITSS Document RAD.NEDL.OC.
- O'Reilly J.E., Maritorena S., Mitchell B.G., Siegel D.A., Carder K.L., Garver S.A., Kahru M., and McClain C. 1998, "Ocean color chlorophyll algorithms for SeaWiFS", *J. Geophys. Res.*, 103, pp. 24,937-24,953.
- Robins, D.B., A.J. Bale, G.F. Moore, N.W. Rees, S.B. Hooker, C.P. Gallienne, A.G. Westbrook, E. Maranon, W.H. Spooner, and S.R. Laney (1996). AMT-1 cruise report and preliminary results. NASA Tech. Memo. 104566, Vol. 35. S.B. Hooker and E.R. Firestone, Eds., NASA Goddard Space Flight Center.
- Shettle, E.P., and R.W. Fenn (1979). Models for the aerosols of the lower atmosphere and the effects of humidity variations on their optical properties. Air Force Geophys. Lab., Hanscom AFB, MA, AFGL-TR-79-0214.
- Stumpf, R.P., V. Ransibrahmanakul, R.A. Arnone, K. Carder, D. Steward, J.R. Pennock, P.A. Tester, M.L. Frayer, and C. Tomas (1998). SeaWiFS ocean color algorithms for turbid coastal waters of the U.S. southeast. In *Proceedings of the Fifth International Conference on Remote Sensing for Marine and Coastal Environments*, Vol. I, p. 141.
- Tassan, S. (1994) "Local algorithms using SeaWiFS data for the retrieval of phytoplankton pigments, suspended sediment, and yellow substance in coastal waters," *Appl. Opt.*, Vol. 33, 2369-2378.
- Vasilkov A.P. 1999, Raytheon ITSS Document CAL.ARA.OC.
- Vasilkov A.P., V.I. Burenkov, and K.G. Ruddick (1998). The spectral reflectance and transparency of river plume waters. *International Journal of Remote Sensing*, 20, pp. 2497-2508.

- Wang M. (1999). Atmospheric correction of ocean color sensors: computing atmospheric diffuse transmittance. *Applied Optics*, 38, pp. 451-455.
- Wang M. (2002). The Rayleigh lookup tables for the SeaWiFS data processing: accounting for the effects of ocean surface roughness. *International Journal of Remote Sensing*, 23, pp. 2693-2702.
- Wang M. (2004). Extrapolation of the aerosol reflectance from the near-infrared to the visible: the single-scattering epsilon vs multiple-scattering epsilon method. *International Journal of Remote Sensing*, 25, pp. 3637-3650.
- Yang H., and H.R. Gordon (1999). Remote sensing of ocean color: assessment of water-leaving radiance bidirectional effects on atmospheric diffuse transmittance. *Applied Optics*, 36, pp. 7887-7897.